NAVAL POSTGRADUATE SCHOOL

MONTEREY, CALIFORNIA

THESIS

BUBBLE CLOUD EFFECT ON LOW- TO MID-FREQUENCY SOUND PROPAGATION IN MOBILE BAY, AL

by

Jeremy Bullard

June 2023

Thesis Advisor: Davis B. Reeder
Second Reader: John E. Joseph

THIS PAGE INTENTIONALLY LEFT BLANK

REPORT DOCUMENTATION PAGE	*Form Approved OMB No. 0704-0188*

1. AGENCY USE ONLY *(Leave blank)*	**2. REPORT DATE** June 2023	**3. REPORT TYPE AND DATES COVERED** Master's thesis

4. TITLE AND SUBTITLE
BUBBLE CLOUD EFFECT ON LOW- TO MID-FREQUENCY SOUND PROPAGATION IN MOBILE BAY, AL

5. FUNDING NUMBERS
RQPQ9

6. AUTHOR(S) Jeremy Bullard

7. PERFORMING ORGANIZATION NAME(S) AND ADDRESS(ES)
Naval Postgraduate School
Monterey, CA 93943-5000

8. PERFORMING ORGANIZATION REPORT NUMBER

9. SPONSORING / MONITORING AGENCY NAME(S) AND ADDRESS(ES)
Office of Naval Research (Code 32) One Liberty Center, 875 N. Randolph Street, Suite 4125, Arlington, VA 22203

10. SPONSORING / MONITORING AGENCY REPORT NUMBER

11. SUPPLEMENTARY NOTES The views expressed in this thesis are those of the author and do not reflect the official policy or position of the Department of Defense or the U.S. Government.

12a. DISTRIBUTION / AVAILABILITY STATEMENT
Approved for public release. Distribution is unlimited.

12b. DISTRIBUTION CODE
A

13. ABSTRACT (maximum 200 words)

The Mobile Bay Estuary Acoustic Field Experiment 2021 (MBE2021) was funded by the Office of Naval Research (ONR) as part of the multi-university Undersea Remote Sensing (USRS) program directed by Dr. Reginald Beach (ONR 322). During the experiment, environmental and acoustic data were collected June 9–15, 2021, in the vicinity of the mouth of Mobile Bay, AL, focused on assessing the impact on acoustic propagation by tidal fronts. A linear frequency-modulated acoustic signal from 500–5000 Hz was transmitted throughout the tidal cycle. This signal was measured by multiple moored receivers to determine the energy that passed between the source and receiver before, during, and after frontal passage. Nominal variations due to changes of acoustic ray paths were ~4 dB. During periods of frontal passage, decreases of ~7 dB were observed over the scale of minutes. This increase in transmission loss is likely due to bubbles carried by the tidal front. ROMS model predictions indicate that a submerged sound channel exists for ~1 hour during the tidal ebb, creating a depth-dependent feature that supports extended propagation ranges. These physical factors indicate that the tidal front can create an exploitable submerged sound channel, while at the same time transmission through the front will experience additional loss beyond what is currently modeled.

14. SUBJECT TERMS
acoustic propagation, acoustics, Mobile Bay, estuarine front, bubble, soundscape

15. NUMBER OF PAGES
79

16. PRICE CODE

17. SECURITY CLASSIFICATION OF REPORT	**18. SECURITY CLASSIFICATION OF THIS PAGE**	**19. SECURITY CLASSIFICATION OF ABSTRACT**	**20. LIMITATION OF ABSTRACT**
Unclassified	Unclassified	Unclassified	UU

NSN 7540-01-280-5500

Standard Form 298 (Rev. 2-89)
Prescribed by ANSI Std. 239-18

THIS PAGE INTENTIONALLY LEFT BLANK

Approved for public release. Distribution is unlimited.

BUBBLE CLOUD EFFECT ON LOW- TO MID-FREQUENCY SOUND PROPAGATION IN MOBILE BAY, AL

Jeremy Bullard
Lieutenant Commander, United States Navy
BS, Maine Maritime Academy, 2013

Submitted in partial fulfillment of the
requirements for the degree of

MASTER OF SCIENCE IN METEOROLOGY AND PHYSICAL OCEANOGRAPHY

from the

NAVAL POSTGRADUATE SCHOOL
June 2023

Approved by: Davis B. Reeder
Advisor

John E. Joseph
Second Reader

Peter C. Chu
Chair, Department of Oceanography

THIS PAGE INTENTIONALLY LEFT BLANK

ABSTRACT

The Mobile Bay Estuary Acoustic Field Experiment 2021 (MBE2021) was funded by the Office of Naval Research (ONR) as part of the multi-university Undersea Remote Sensing (USRS) program directed by Dr. Reginald Beach (ONR 322). During the experiment, environmental and acoustic data were collected June 9–15, 2021, in the vicinity of the mouth of Mobile Bay, AL, and focused on assessing the impact on acoustic propagation by tidal fronts. A linear frequency-modulated acoustic signal from 500–5000 Hz was transmitted throughout the tidal cycle. This signal was measured by multiple moored receivers to determine the energy that passed between the source and receiver before, during, and after frontal passage. Nominal variations due to changes of acoustic ray paths were ~4 dB. During periods of frontal passage, decreases of ~7 dB were observed over the scale of minutes. This increase in transmission loss is likely due to bubbles carried by the tidal front. ROMS model predictions indicate that a submerged sound channel exists for ~1 hour during the tidal ebb, creating a depth-dependent feature that supports extended propagation ranges. These physical factors indicate that the tidal front can create an exploitable submerged sound channel, while at the same time transmission through the front will experience additional loss beyond what is currently modeled.

THIS PAGE INTENTIONALLY LEFT BLANK

TABLE OF CONTENTS

THIS PAGE INTENTIONALLY LEFT BLANK

LIST OF FIGURES

THIS PAGE INTENTIONALLY LEFT BLANK

LIST OF TABLES

THIS PAGE INTENTIONALLY LEFT BLANK

LIST OF ACRONYMS AND ABBREVIATIONS

ADCP	Acoustic Doppler Current Profiler
AIS	Automated Identification System
APL	Applied Physics Laboratory
ASW	anti-submarine warfare
BRSR	bottom-reflected-surface-reflected
CB	R/V Caillou Boca
CNO	Chief of Naval Operations
CP	R/V Coastal Profiler
CTD	conductivity temperature depth
Fs	sampling frequency
H&H	Harrison and Harrison
IVO	in the vicinity of
L2MF	low-to-mid-frequency
LFM	Linear Frequency Modulated
LUMCON	Louisiana University Marine Consortium
Mab	meters above bottom
MAVS	Modular Acoustic Velocity Sensor
METOC	Meteorology and Oceanography
MOB	Mobile Bay
NaN	not a number
NDBC	National Data Buoy Center
NRL	Naval Research Laboratory
ONR	Office of Naval Research

OSU	Oregon State University
PAH	Pass aux Herons
PMAP	Protective Measures Assessment Protocol
PSD	Power Spectral Density
RBR	refracted-bottom-reflected
ROMS	Regional Ocean Modeling System
RR	refracted-refracted
RSR	refracted-surface-reflected
TL	transmission loss
USCG	United States Coast Guard
USRS	Undersea Remote Sensing
WHOI	Woods Hole Oceanographic Institute

ACKNOWLEDGMENTS

First and foremost, I must thank my wife Anne for tolerating all the time I spent working throughout this process.

Thank you, Dr. Ben Reeder and John Joseph, for all of your assistance. From getting the equipment ready for the field through the writing process, you both have been with me throughout my entire time at NPS. I would not have been able to complete this project without your support and guidance.

A shout-out to Tarry Rago for his detailed notes, which I needed to refer to on multiple occasions throughout the writing process.

Just like every student passing through the oceanography program, I owe thanks to Mike Cook for his assistance with MATLAB programming and the roadblocks I ran into.

THIS PAGE INTENTIONALLY LEFT BLANK

I. INTRODUCTION

A. MOTIVATION

The Chief of Naval Operations (CNO) states in his NAVPLAN (2021) that the priorities for the Navy are Distributed Maritime Operations, Littoral Operations in a Contested Environment, and Expeditionary Advanced Base Operations (Gilday 2021). For the Navy to be able to support these three objectives, we must first understand the environment. More specifically, the meteorology and oceanography (METOC) community must be able to accurately forecast the nearshore environment. Regions where water masses meet are highly dynamic and complex to model (Geyer and MacCready 2014; Ralston et al. 2017; Reeder and Lin 2019; Warner et al. 2005). There is not one typical nearshore region, as such an understanding of a wide range of nearshore interactions is important to be able to model different regions accurately (Geyer and MacCready 2014). Under the Undersea Remote Sensing (USRS) program, multiple estuaries were investigated to determine appropriate parameterization for a range of estuaries (Figure 1). In addition to being a more complex environment, estuaries have an active and diverse ecology. With the presence of marine pinnipeds and cetaceans, the Navy can be limited in operational frequency bands and acoustic intensity levels that are authorized under the Protective Measures Assessment Protocol (PMAP). Beyond limiting frequencies and source levels the Navy can use, marine life also adds to the background noise levels, making discernment of signals of interest more complicated.

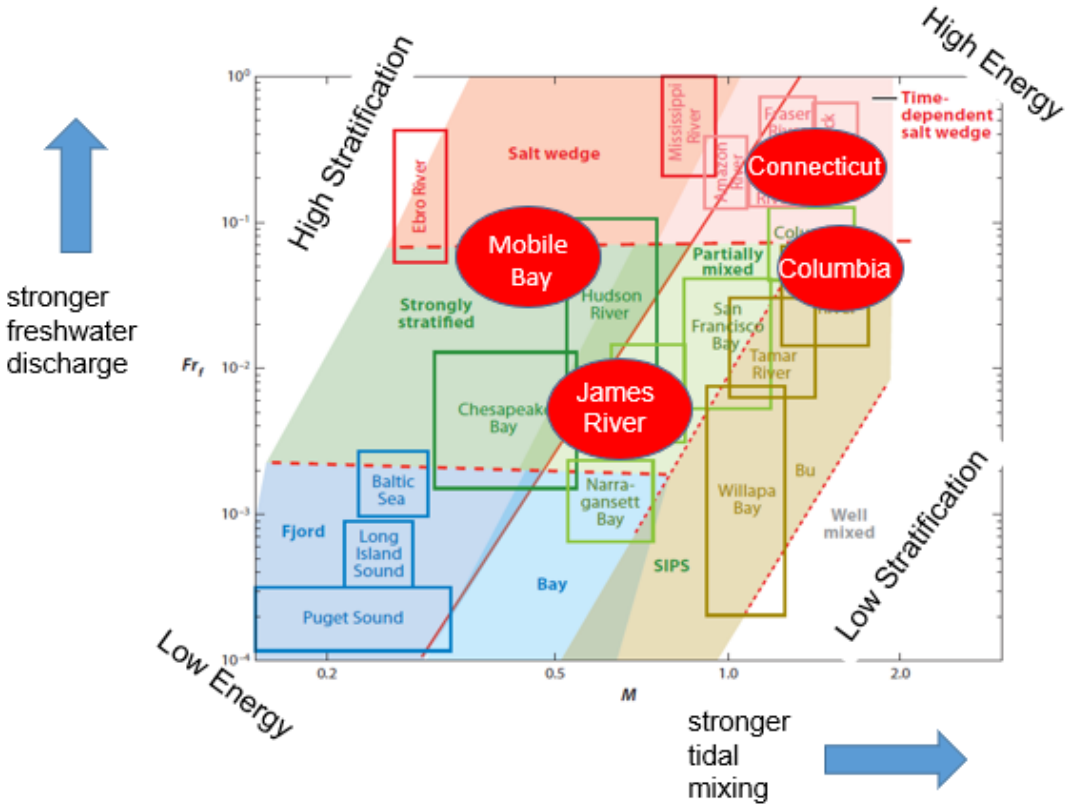

Figure 1. Energy and stratification diagram for estuary systems. Systems investigated by the USRS program are displayed in red circles. Adapted from Geyer and MacCready (2014).

B. PROBLEM

While many studies historically have focused on tides, salinity, temperature, and currents, the Navy needs to expand its use of acoustics to characterize and understand the ocean environment, particularly in constrained, energetic environments like estuaries more fully. In a horizontally stratified ocean, four waveguide paths of acoustic propagation are typically considered: refracted-refracted (direct path) (RR), bottom-reflected-surface-reflected (bottom bounce) (BRSR), refracted-surface-reflected (surface duct) (RSR), and refracted-bottom-reflected (RBR) (Lurton 2010). Typical energy losses of sound traveling through the water along these paths include spherical spreading, cylindrical spreading, surface scattering loss, and bottom loss (Lurton 2010; Medwin 2005; Urick 1996). Models focus on these mechanisms; traditional 2D models consider frequency, vertical refraction,

bottom loss, and surface scattering, with spreading being accounted as a function of range (Ainslee 2005; Novarini et al. 1998).

Currently, most unmanned systems use high frequency acoustics for navigation and communication (Thurman et al. 2013). While these systems have high fidelity, their ranges are limited as the high frequency signals (i.e., 10–100s kHz) attenuate significantly with range (Bassett and Lavery 2021; Lurton 2010). One cause of the significant attenuation at these higher frequencies can be air bubbles in the water column (Reeder et al. 2022). These bubbles can come from a variety of sources including breaking waves, rainfall, at the leading edge of internal solitary waves, and at estuarine fronts (Blenkinsopp and Chaplin 2007; Leighton 1997; Reeder et al. 2019; Reeder et al. 2022). In a bubbly mixture, acoustic signals at lower frequencies are less attenuated than at higher frequencies; lower frequency signals are therefore less susceptible to bubbles in the water column (Bassett and Lavery 2021; Lurton 2010; McDaniel and Gormon 1982). Although less attenuated, low-to-mid-frequencies (L2MF) (500-5000 Hz) can still be influenced by bubbles in the water column (Ainslee 2005; Novarini et al. 1998; Reeder et al. 2022). The U.S. Navy uses signals in the L2MF band for anti-submarine warfare (ASW) from surface vessels (D'Amico and Pittenger 2009). Even without expanding beyond current capabilities, this direct connection to ASW demonstrates that a better understanding of L2MF acoustic propagation in environments with bubbles is required by the Navy.

The two dominant bubble generation mechanisms are breaking waves and rainfall (Farmer 1984). These bubbles often are localized near the surface of the water due to buoyancy and minimal downward velocity (Bassett and Lavery 2021; Chua et al. 2018; Dahl et al. 2008). With a strong downwelling velocity (e.g., caused by Langmuir circulation in open water), some bubbles become entrained to several meters depth; however, 95% of the entrained air is lost over one wave period (Blenkinsopp and Chaplin 2007; Lamarre and Melville 1991). Another ocean feature causing bubble entrainment into the water column occurs at the tidal fronts between water masses with differing characteristics. At these estuarine fronts where the two water masses collide, breaking waves are often formed, and bubbles are entrained into the near-surface waters. The bubbles are subsequently subducted to depth by the negative current velocities associated

with the denser, plunging salt water (Baschek et al. 2006; Farmer et al. 2002; Reeder et al. 2018).

Few acoustic propagation models include the effects from bubbles; of those that do most models use generic bubble parameterizations and are not realistic about how bubbles are distributed (Novarini and Bruno 1982; Novarini et al. 1998; Reeder and Lin 2019). Typically, there is a large degree of spatial variance in bubble density, causing a high degree of localized variance in transmission loss (TL) along an acoustic transect, rather than as one constant value used for a model (Ainslee 2005). The mechanisms that are not accounted for in most models include bubble scattering, bubble absorption, enhanced surface interaction caused by lower effective sound speeds in the near-surface bubbly mixture, horizontal refraction, and enhanced seabed roughness (Ainslee 2005; Lurton 2010; Medwin 2005; Urick 1996).

In addition to the propagation of the sound signal the user is interested in measuring, background energy is present in the water column. This energy, or background noise, can be significant and makes measuring a desired signal difficult. One component of background noise that can dramatically influence the ability to receive signals is shipping traffic. Ships typically create noise at 100s of Hz, decreasing above 500 Hz at a rate of ~6 dB per octave (Leighton 1997; Lurton 2010). While this typically the case in deep water, ships in shallow water are known to contribute energy across a wider frequency band beyond 500 Hz, particularly at short ranges (Leighton 1997, Reeder et al. 2020).

For an acoustic model to be realistic, it must account for the water column properties, bottom sediment characteristics, sound energy propagation paths, and external energy sources. Given the energetic dynamics of environments like estuaries, models must be created to a fine grid spacing. Typical models ignore air bubbles or treat their presence with a simple parameterization of loss near the surface. To facilitate model development, real-world data collection must be conducted. With both the model and real-world data analysis being completed, acoustic models can then be applied and compared to other dynamic areas with different properties to ensure accurate predictions.

C. GOALS

The focus of the field campaign within the USRS was to use acoustics to better understand, map, and quantify 4D underwater structures of frontal zones and non-hydrostatic processes in Mobile Bay (MOB) (Figure 2). The specific objective of the research in this thesis was to compare L2MF acoustic data with high resolution TL models to characterize the acoustic propagation environment of MOB (Figure 2).

Figure 2. Google Earth imagery of Mobile Bay, red box indicates study area. Two paths of water to flow into MOB are marked with white text.

THIS PAGE INTENTIONALLY LEFT BLANK

II. BACKGROUND

A. ENVIRONMENT

Estuaries can be defined through different metrics, and include environments from sounds, fjords, bays, to river mouths (Figure 1). Most simply, estuaries are regions in which outflowing fresh water meets a salty water mass (Reeder 2016; Reeder et al. 2020). These areas are highly dynamic, tending to have a variety of complex forcing mechanisms in addition to tidal influences (Geyer and MacCready 2014). This exchange is comprised of an outflowing fresh water layer near the surface and salt water flowing into the waterway at depth (Geyer and MacCready 2014). The fresh water entering the estuary often forms a layer 1–3 m thick on top of the denser salt water (Dzwonkowski et al. 2014; Reeder et al. 2018).

Mobile Bay is ~55 km long and an average of 17 km wide. The depths within MOB are ~3 m throughout the bay, except for a shipping channel that is dredged and maintained 14 m deep and 120 m wide (Kim and Park 2012; Lee et al. 2013). Mobile Bay receives runoff from the Mobile-Tensaw River system, which is the fourth largest river discharge by volume and sixth largest discharge region in the United States (Lee et al. 2013). River discharge into MOB is ~1800 $m^3 s^{-1}$ (Dzwonkowski et al. 2014; Lee et al. 2019; Schroeder et al. 1990). This discharge creates a strong ebb current, which has been known to exceed 1 $m s^{-1}$, though the typical tidal range is <0.5 m (Lee et al. 2013; Lee et al. 2019; Schroeder et al. 1990). During flood tide, the convergence of the ocean tide with the river outflow creates a converging, bathymetrically-driven system of fronts near Mobile Point known as the “Dixey V” (Figure 3).

Mobile Bay has two straits through which salt water enters. The Pass aux Herons (PAH) enables water to flow in from the Mississippi Sound, while the main pass lets water flow from the Gulf of into Mobile Bay. These two paths result in a distinct flow pattern within MOB, where Dauphin Island prevents direct flow between these two straits, causing a phase lag for flow into and out of MOB (Lee et al. 2019). Approximately 86% of the flow passes through the main pass, with the remaining 14% passing through PAH (Lee et al.

2013). As the flooding tide converges with the river outflow through the mouth of Mobile Bay, a "fan" of multiple fronts is created north of Dixey Bar near Mobile Point. These fronts can be seen visually (Figure 3). Though tidal flow can be considered during periods of calm weather, rapid changes to bathymetry, and thus flow, can occur following violent storms such as hurricanes (Orescanin et al. 2016; Flocks et al. 2017).

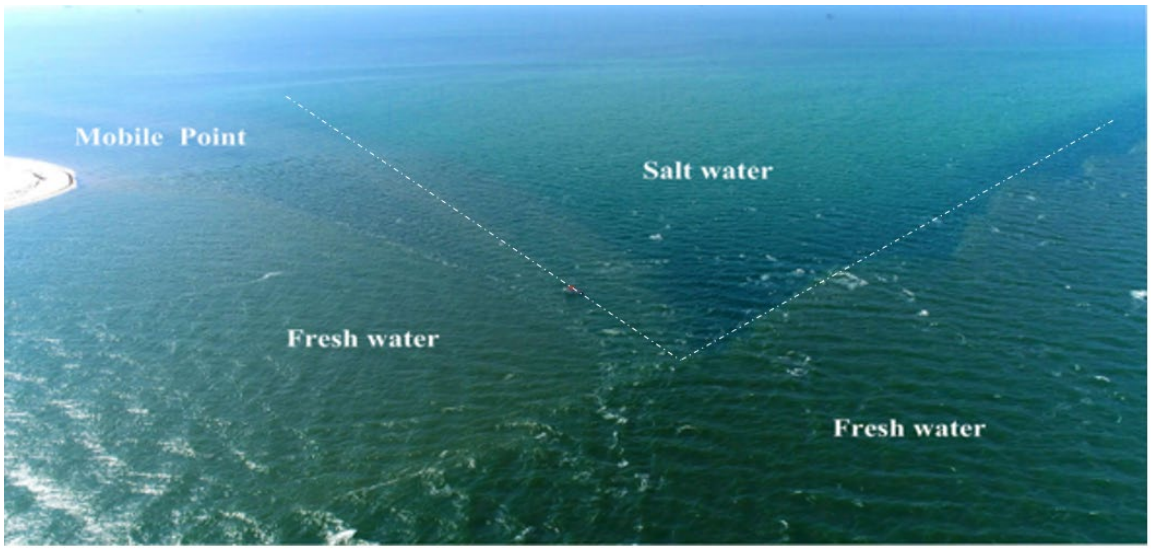

Figure 3. Drone photo taken by OSU operator showing the "Dixey V" formed at the mouth of Mobile Bay. Dashed line to emphasize shape of "Dixey V."

B. EXPERIMENT

1. USRS Program

The Mobile Bay Estuary Acoustic Field Experiment 2021 (MBE2021) was funded by the Office of Naval Research (ONR) as part of the multi-university USRS program directed by Dr. Reginald Beach (ONR 322). The entities involved in the study included the Applied Research Laboratory at the University of Texas Austin, Applied Physics Laboratory (APL) University of Washington, Naval Postgraduate School (NPS), Naval Research Laboratory (NRL), Oregon State University (OSU), and Woods Hole Oceanographic Institute (WHOI). This project represented the fifth and final field experiment under the USRS program over the past six years to investigate and determine

better ways to quantify the underwater structure of estuaries with different energy and stratification (Figure 1). The focus of this field experiment was understanding the nearshore oceanographic environment near the entrance to Mobile Bay, between Fort Gaines on Dauphin Island to the west and Mobile Point to the east (Figure 2). Prior to the experiment, NRL conducted a hydrographic survey of the region to ensure the team had updated bathymetry for the region prior to equipment deployment and to improve model boundaries (Figure 4). OSU installed and operated an X-band radar backscatter system near Mobile Point, providing characterization of surface roughness in the region, as well as live imagery throughout the campaign (Lyzenga 1991). In addition to high-frequency ship- and AUV-borne acoustic systems, acoustic equipment deployed by NPS included a moored source and a series of moored receivers to characterize L2MF acoustic propagation through the bubble-laden fronts.

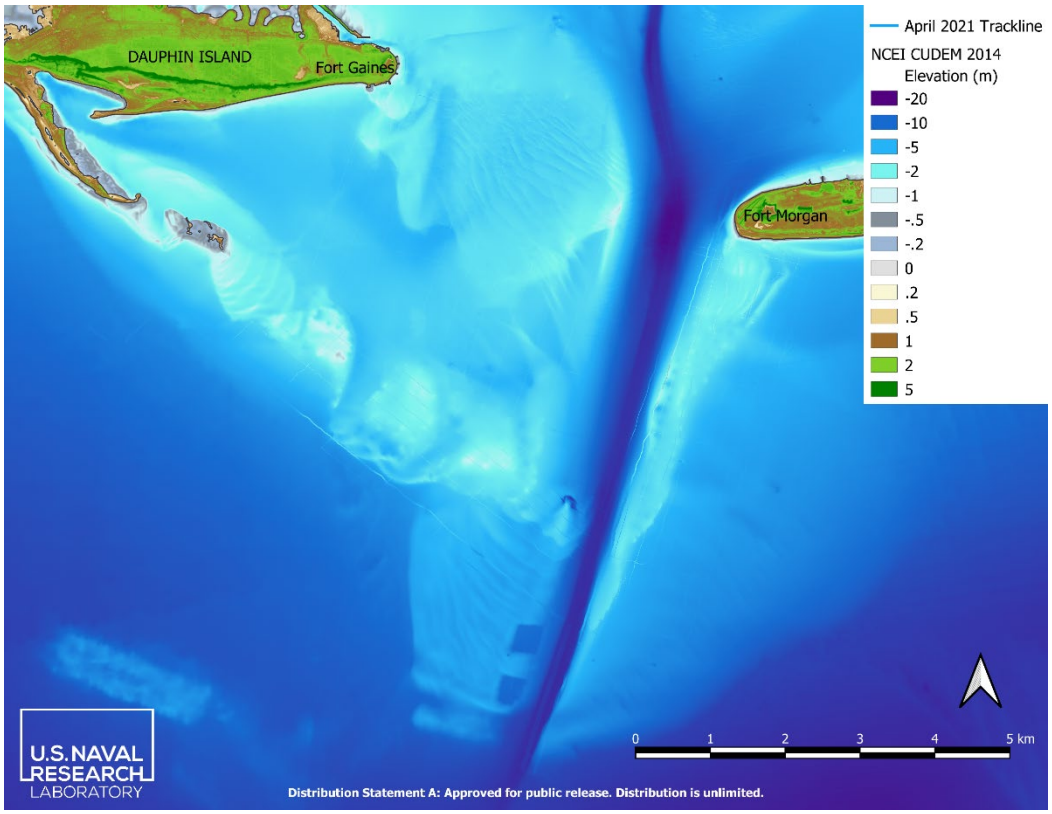

Figure 4. NRL hydrographic survey data. Survey was completed in April 2021. Source: Harrison et al. (2021).

2. Ship and Schedule

The experiment lasted for two weeks, June 5–18, 2021. The NPS team mobilized equipment that had been shipped to the area June 5–7, 2021. Louisiana University Marine Consortium (LUMCON) provided vessels for all involved research teams during the field experiment. The NPS team used two vessels over the course of the experiment. The first vessel used was the R/V Coastal Profiler (CP), a 41x16-foot Lafitte style skiff, used June 7–12 (Figure 5). The CP was outfitted with a winch system to aid with launching and recovering equipment. Equipment testing and practice launching/recovering of equipment was conducted on June 7 inside MOB to limit surface waves while the team established the best launch/recovery sequence for all equipment.

When returning to port on June 12, the R/V Coastal Profiler experienced a mechanical issue that prevented her further use during the project. LUMCON provided the R/V Caillou Boca (CB), a 24-foot Boston Whaler style craft (Figure 6). The CB was not large enough to launch the Lubell source and lacked a winch system to recover the Lubell source. Due to this limitation with CB, data collection for June 12–15, 2021, lacked an active source. The underway times throughout the experiment were restricted to the daytime hours of 1200–1700Z (Appendix). This timeframe was characterized by an ebb tide during the beginning of the experiment, and a flood tide at the end of the experiment (Figure 7).

Figure 5. R/V Coastal Profiler

Figure 6. R/V Caillou Boca

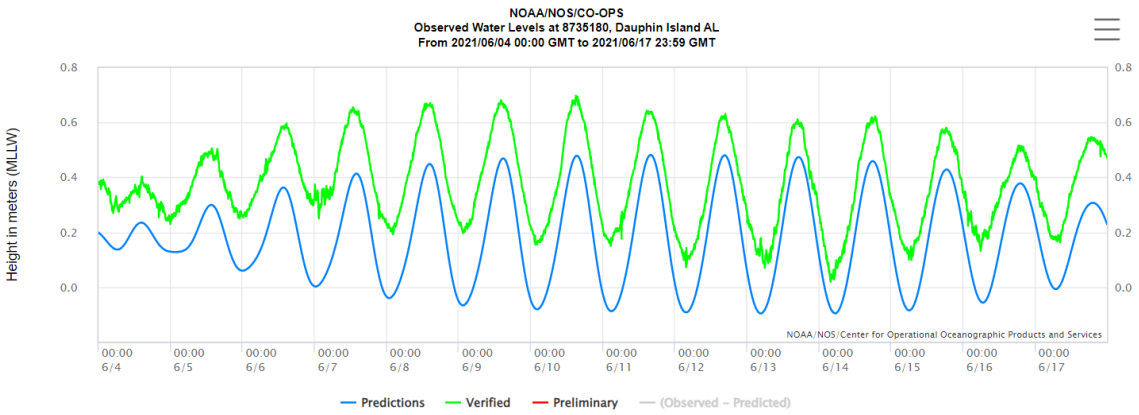

Figure 7. NOAA tide data for Dauphin Island, AL. Source: NOAA Tides: https://tidesandcurrents.noaa.gov/waterlevels.html?id=8735180&units=standard&bdate=20210601&edate=20210630&timezone=GMT&datum=MLLW&interval=6&action=.

3. Receivers

Receivers were on stationary moorings near the bottom of the water column. These were built using threaded galvanized pipes. The spokes of the moorings were three feet long, with the center coupling being either a 5- or 6-way split (Figure 8). Each spoke was mounted with a 6-inch nipple and 3-inch flange underneath it, to ensure the height was the same at each corner. Each mooring was mounted with different equipment, summarized in Table 1, based on the desired data to be obtained at each location. A 45 lb weight was included under the center of each mooring. Two 45 lb weights were used on R2. A Nobska Modular Acoustic Velocity Sensor (MAVS) was the only equipment deployed at R2, near the strongest expected currents, with the objective of measuring the local currents directly in the mouth of the bay. The extra weight was meant to ensure stability of the mooring and prevent the MAVS from tipping over in the energetic currents expected at this location. A buoy was used to mark the location of each mooring and ensure visibility for recovery. This buoy was attached to a 20 lb anchor and connected via a 25 m tether line to the receiver. The tether line was used to minimize the current drag effect on equipment attached to the moorings.

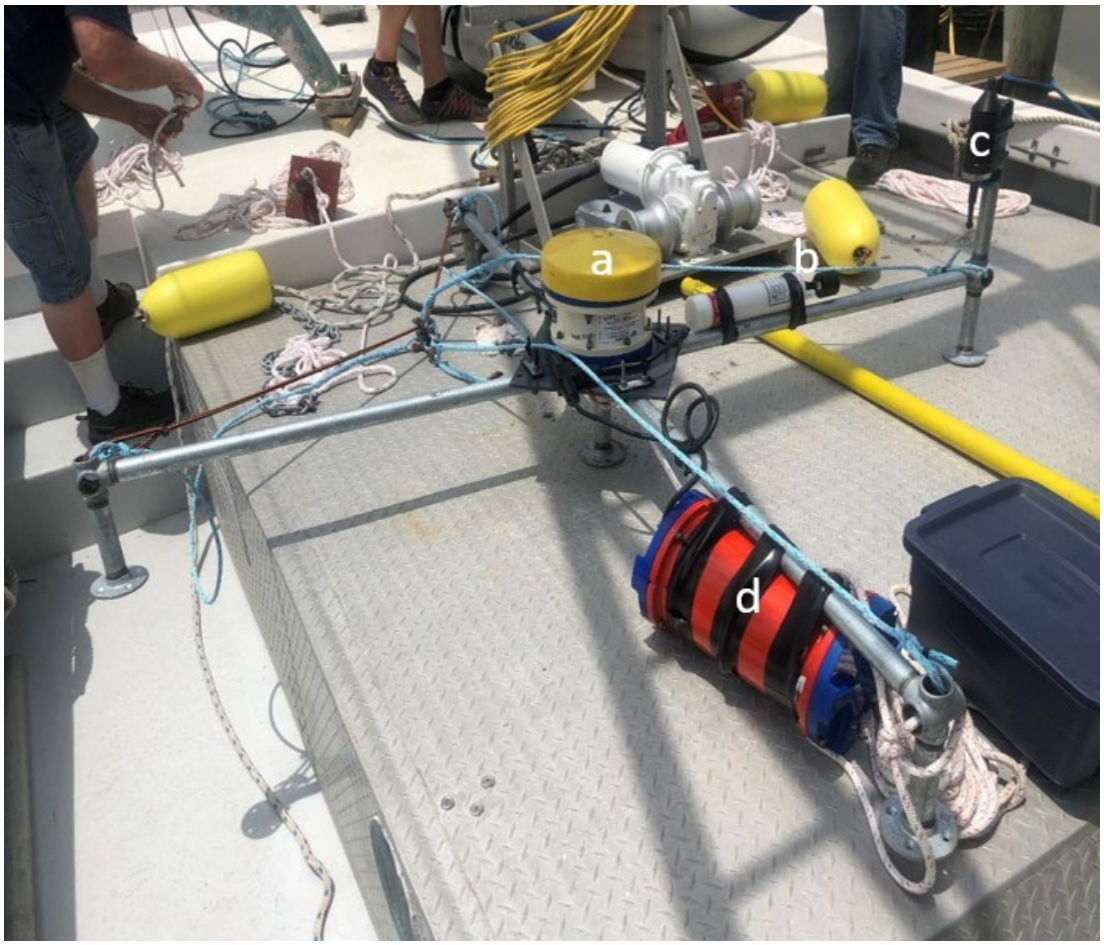

Figure 8. Example of receiver set up with a) acoustic doppler current profiler (ADCP), b) RBR conductivity temperature depth (CTD) sensor, c) Acousonde, and d) battery source

Table 1. Equipment list with deployment location

Mooring	Equipment	Serial Number	Lat/Long
R1	RBR-CTD MAVS Acousonde ADCP	60318 10320 A050 2595	30°14.806'N 088°01.932'W
R2	MAVS	10307	30°13.587'N 088°01.870'W
R3	RBR-CTD ADCP ST300	60315 7819 6222	30°12.864'N 088°00.842'W
R4	RBR-CTD ADCP ST300	60319 7290 6235	30°12.154'N 088°01.207'W
R5	RBR-CTD Acousonde	205305 A066	30°13.086'N 088°01.995'W
Source		Date	Lat/Long
		09June2021	30°11.324'N 088°01.641'W
		10June2021	30°11.324'N 088°01.641'W
		11June2021	30°15.726'N 088°01.878'W
		12June2021	30°15.746'N 088°01.823'W

4. Source

The L2MF source was designed to be stationary and remain near the bottom, to facilitate investigation of acoustic travel time through the bubble-laden estuarine fronts. The primary source was Lubell Lab's high-power broadband piezoelectric underwater acoustic transducer (LL1424-HP). The Lubell source was mounted to a fiberglass "spider" mooring with 50 lb weights bolted on each foot (Figure 9). The Lubell was powered and

controlled via cable from the "COFFIN" (described below) mounted on a floating platform at the surface. A swivel mount was placed between the source frame and the tripod to prevent the connection cable from twisting.

The first-generation COFFIN was developed during the James River Experiment (JRE2019) and improved for this experiment (Rogers 2020). The COFFIN contained the following equipment: three 12 V marine batteries, a Siglent 1032X Signal Generator, Crown CDi6000 source amplifier, a Lubell bridge, and a Trimble GPS receiver (Figure 10). The COFFIN was kept afloat on a Roanoke inflatable, 8-foot pontoon boat (Figure 11). The Trimble GPS receiver provided GPS time for the signal initiation. An Automated Identification System (AIS) (serial number 941204463) marker was added to the pontoon boat the last three days of the experiment to allow the research team to monitor the location of the source while conducting experimental operations farther from the source. The Lubell transmitted 1-second-long linear frequency modulated (LFM) signals in the 500–5000 Hz band; these signals were generated by the Siglent 1032X Signal Generator every two seconds (50% duty cycle) at an approximate source level of 180 dB re 1μPa at 1 m. PVC pipes were added through the top of the COFFIN to act as splash screens, while allowing ventilation. Foil was added to the outside of the COFFIN to reflect solar radiation and prevent the equipment from overheating.

Figure 9. Lubell source on fiberglass mooring. The mooring was held in place with 50 lb weights bolted onto each leg.

Figure 10. COFFIN interior with a) GPS, b) waveform generator, c) three batteries, d) amplifier, e) Lubell bridge, f) inverter, and g) cooling fan.

Figure 11. COFFIN on Roanoke pontoon boat after deployment, moored above acoustic source. On each edge of the COFFIN are radar reflectors and an AIS marker to assist in locating the system at the end of each day.

THIS PAGE INTENTIONALLY LEFT BLANK

III. METHODS AND DATA

A. METHODS

The experiment was conducted from June 5, 2021, to June 18, 2021, with data collected by the NPS team during June 9–15. Equipment was deployed from 4 km north to 10 km south of Mobile Point (Figure 12). The source was deployed around the diurnal high tide, based on the estimated high tide from the tide station located at Dauphin Island, AL (Tide station #8735180). The tidal range over the course of the experiment was -0.2 m to +0.5 m (Figure 7).

Two receivers, R3 and R4, were deployed on June 8, and the remaining receivers R1, R2, and R5 were deployed on June 11. The source was deployed in the vicinity of (IVO) S3 on June 9 and 10, and IVO S1 on June 11 and 12 (Figure 12). The source was recovered at the end of each day. The acoustic receivers, either Acousonde or ST300, were set to record passively throughout the experiment from launch until recovery. Data processing is described in Chapter III C.

All ADCPs were calibrated prior to deployment based on Workhorse manufacturer specifications. Once calibrated, the ADCPs were set to sample at 5 Hz, with data binned in 0.5 m increments from 1.05-10.05 m.

Acoustic model runs were conducted using Bellhop, a ray-based propagation model developed by Mike Porter (Porter 2019). Bellhop uses the following environmental parameters as inputs: bottom sediment density, bottom attenuation, sediment sound speed, water column temperature, water column salinity, and source depth. For this experiment, models were run with 31 cross sections taken from the source to a range of 3.1 km, with 101 receivers spaced vertically at each of these cross sections. Predictions of temperature and salinity along the acoustic transects were supplied from the Regional Ocean Modeling System (ROMS) prepared by Dr. David Ralston at WHOI (Ralston 2022). The ROMS model uses primitive ocean equations, with a base assumption of a hydrostatic environment (Warner et al. 2005). Bottom samples were collected and analyzed by Dr. Shawn Harrison (NRL) (Figure 13). Based on a weighted percentage, the region along the transect between

S3 and R3 was predominantly sand, with values of 98.6%, 98.4%, and 100% at location 16, 33, and 34 respectively. Based on the predominant sediment type being coarse sand, values for density of 2.034 g cm^{-3}, attenuation of 0.660 dB $wavelength^{-1}$, and sound speed of 1836 m s^{-1} were used in the Bellhop model runs (Hamilton 1980).

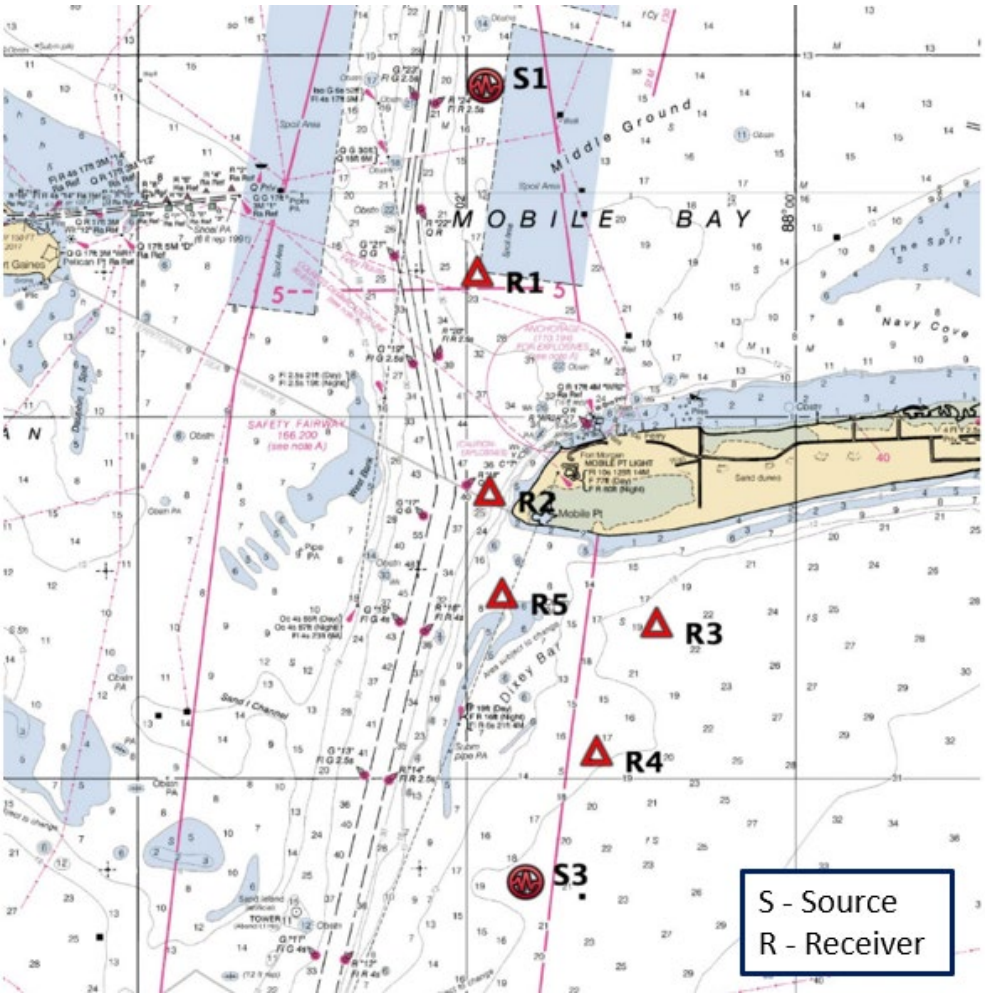

Figure 12. Approximate location of equipment deployed by NPS team.

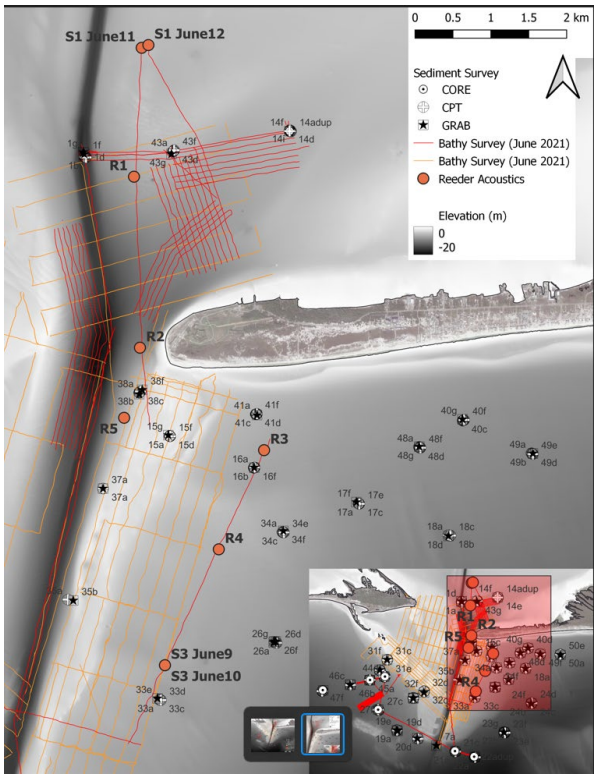

Figure 13. Bottom samples collected and analyzed by NRL. Image provided by Dr. Shawn Harrison (NRL).

B. ENVIRONMENTAL DATA

The top panel of Figure 14 displays wind speed (m s^{-1}) and direction (degrees from true north in color) as a function of time between June 7 and June 17. The bottom panel of Figure 14 displays air temperature in °C for the same period. Wind speed, wind direction and air temperature varied from 4 to 11 m s^{-1}, 150 to 270 degrees, and 22 to 30 °C, respectively, from June 7 to June 13; on June 13, the wind speed decreased to 1 m s^{-1}, the wind direction shifted from 270 to 190 degrees, and the air temperature decreased from 28.6 to 26.1 °C over a 0.25 hour period due to the passage of an atmospheric cold front. Following the passage of the atmospheric front, the wind speed quickly increased to 11 m s^{-1}, the wind direction shifted to 325 degrees and the air temperature increased to 29.8 °C. During the latter third of the observation period, wind speed and direction varied between 1 and 9 m s^{-1} and 090 and 010 deg, respectively, while the air temperature remained between 24 and 30 °C.

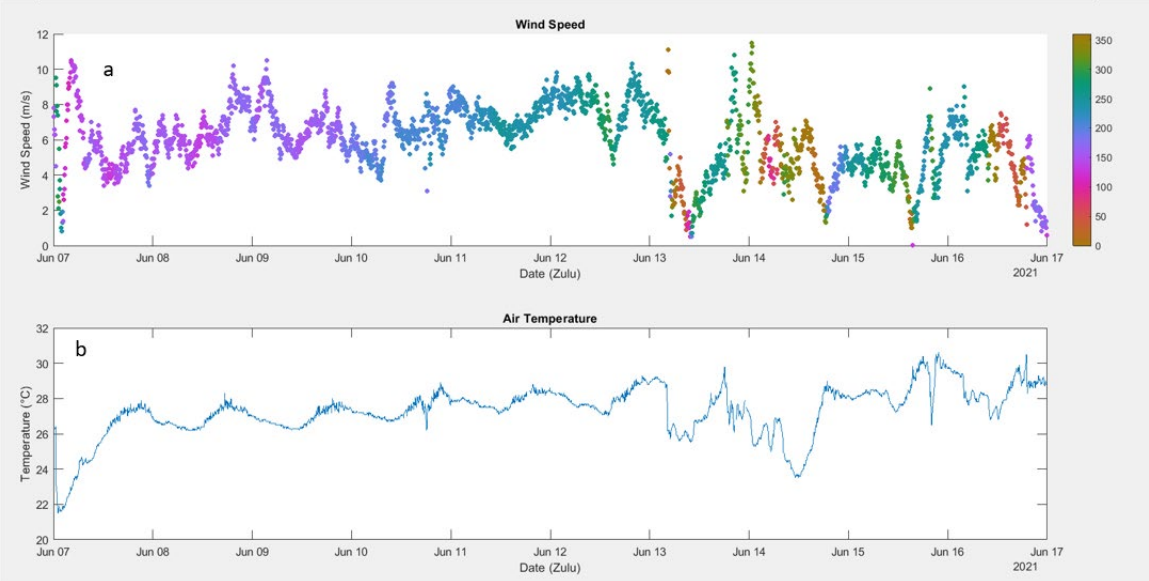

Figure 14. Weather data from NDBC station 8734673 at Fort Morgan, AL. a) Wind velocity with color indicating wind direction b) air temperature.

Three panels depict data collected by Castaway CTD on June 9, 2021, between 1626Z and 1932Z for salinity (PSU), temperature (°C), and sound speed (m s^{-1}) (Figure 15). Data were collected between S3 and R4. The salinity was between 26 and 28 PSU near the surface throughout this period. The salinity data reveals a halocline present from 2–4 m depth, with salinity consistently around 30.5 PSU below 5m. Temperature data presents a warming surface layer from 28.2 °C to a maximum of 28.5 °C. The thermocline sharpens throughout the period, but a mixed layer is present to 3 m depth. Below 3 m, the temperature ranges from 28 °C to 28.1 °C. These two factors account for the sound speed having a range from 1533 m s^{-1} to 1535 m s^{-1} near the surface and increasing to a maximum velocity of 1537 m s^{-1} below 5 m. Sound speed changed the most near the surface during data collection on June 9, when the temperature change was greatest likely due to solar heating.

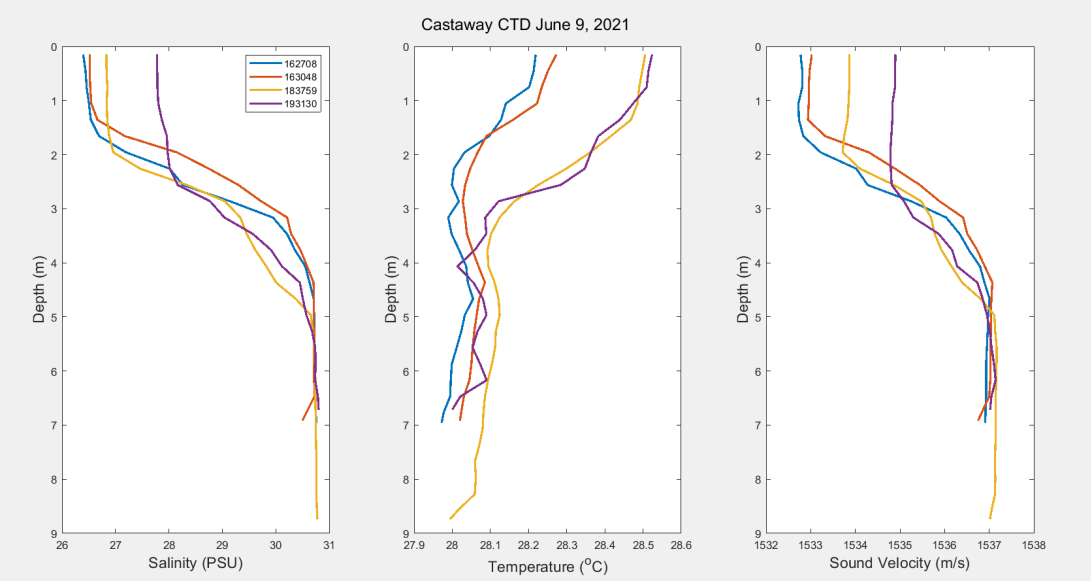

Figure 15. Castaway CTD data from 09JUN202. CTDs were conducted between source and R4 on June 9. Times indicate HHMMSS (GMT)

The temperature of the water, based on RBR-CTD data, can be seen in the upper panel of Figure 16. The water temperature at the beginning of the data collection was ~27.5 °C, decreasing between June 10 and June 12 to a temperature of 24.5 °C. The water remained around 24.5 °C for the rest of the data collection period. Salinity values displayed in the lower panel show a gradual increase from ~32.5 PSU until reaching a maximum value of 34.5 PSU on June 12.

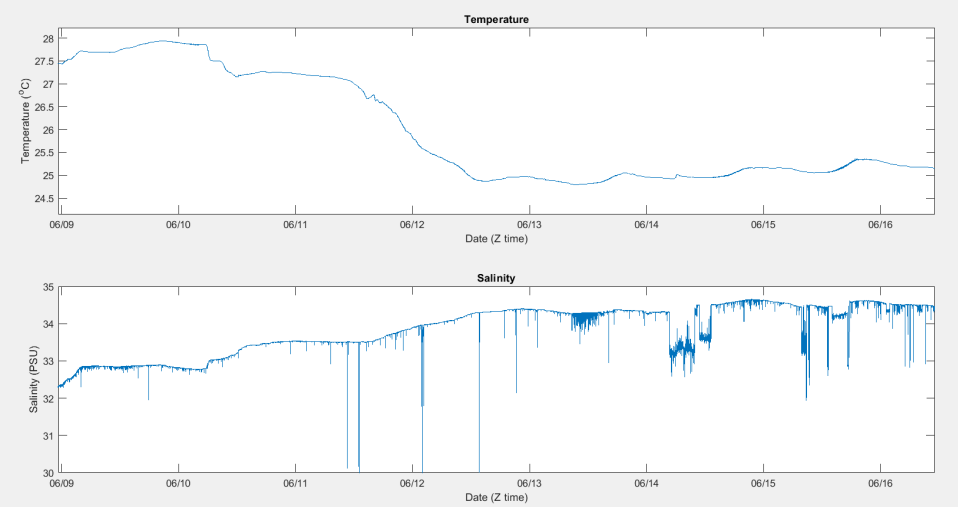

Figure 16. R4 RBR-CTD data plot throughout equipment deployment

Water level data at the Dauphin Island station were used to estimate tidal height. These data give water levels based on sea level and compared with values from RBR-CTDs at R3 and R4. RBR-CTD pressure data were averaged using a 60-second moving window and had the average removed to enable direct comparison of RBR-CTD data to water level changes at Dauphin Island tide gauge (Figure 17). A lag is evident in the pressure between the high and low tides, with Dauphin Island level lagging the level observed at both R3 and R4 near Mobile Point. Initial variance in pressure makes differentiating R3 and R4 values difficult. Variance decreases over the field experiment for the RBR-CTD pressure sensor data, while the Dauphin Island data does not show a similar change in variance over this period.

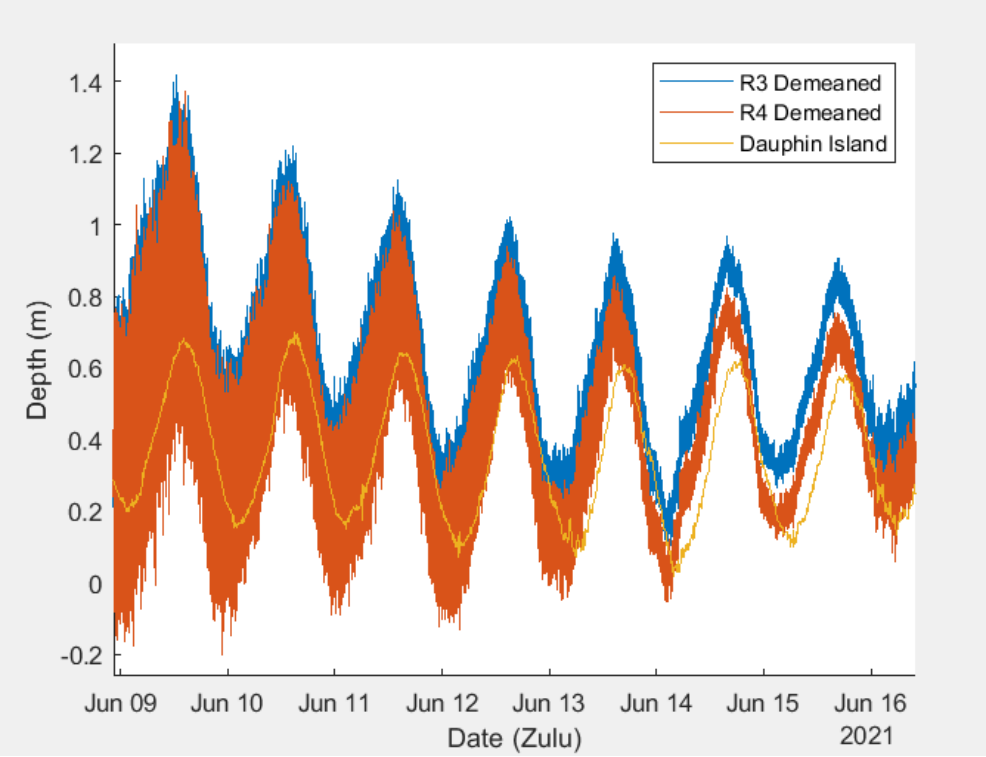

Figure 17. Water level values after removing the mean value. Data for R3 and R4 were taken from RBR-CTD data, while Dauphin Island used data from NOAA Tide Station 8735180.

The dominant wave period seen in the R4 data was 7.1 seconds, or 0.14 Hz between June 9 and 11. This wave period changes from June 11th to June 13th showing two wave periods of 7.1 and 4.2 seconds, or 0.14 and 0.24 Hz, respectively, with red indicating the highest occurrence and blue indicating lowest occurrence (Figure 18).

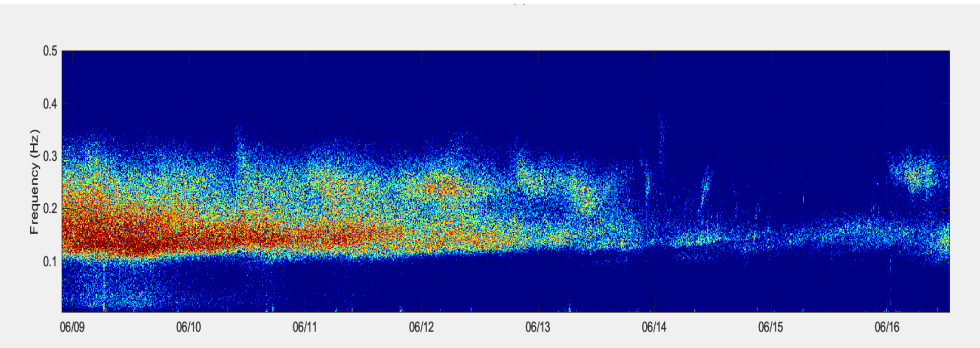

Figure 18. R4 RBR-CTD data with dominant frequency of energy.

Offshore, the wave periods are analyzed at three distinct timeframes: June 9–11, June 11–15, and June 16–17. During the first timeframe, the wave periods were from 6–8 s. These periods decreased to 2–4 s during the second timeframe, prior to increasing back to 6–7 s. Data for the offshore region was derived from National Data Buoy Center (NDBC) buoy 42012 ~47.5 km southeast of MOB measured during the experiment (Figure 19).

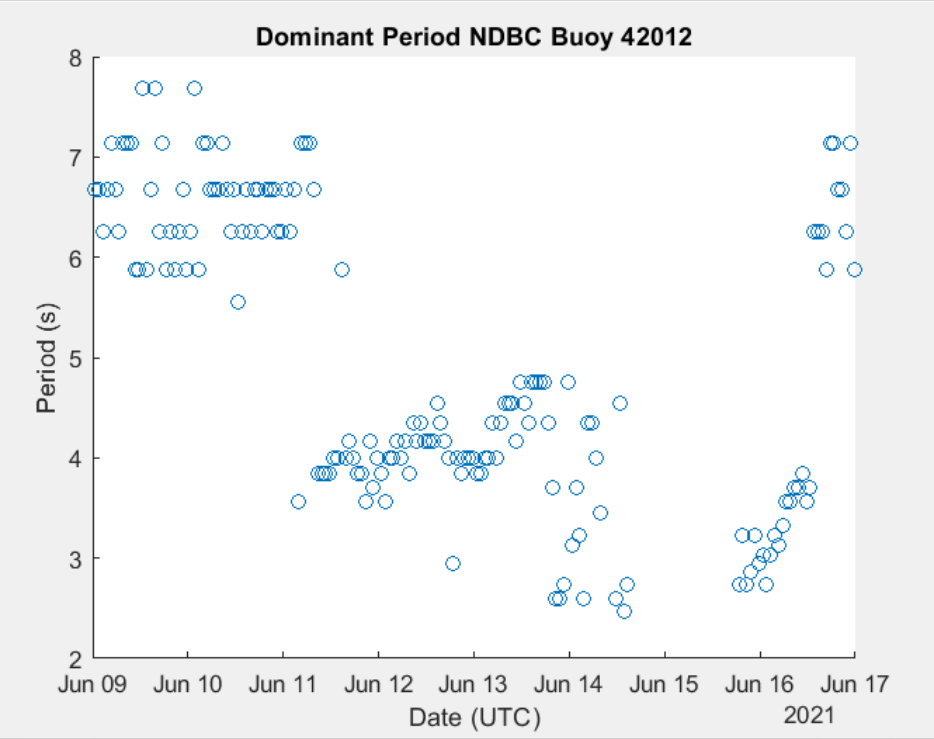

Figure 19. Dominant wave period from NDBC Buoy 42012 at 30°03'36"N 087°32'54"W, ~47.5 km from entrance to MOB.

ADCP data at R4 were analyzed using a 60-second moving average to smooth the data, with 0.5 m bins, similar to Bassett et al. (2013). Values were then calculated for velocities throughout the water column (Figure 20). Flow was broken into east/west (u) and north/south (v) components. The strongest currents appear near the surface, where values reach 0.6 m s^{-1}, while the lower velocity values occur closer to the bottom of the water column. The clearest tidal cycle can be seen in the east/west component near the surface, where values appear to transition diurnally. Near the surface, the east/west

component (u) is the primary driver of water flow, while in the middle of the water column, the north/south component (v) displays comparable values to east/west (u) component. This pattern of flow can be seen at R4 primarily moving in an east/west direction, along the coast.

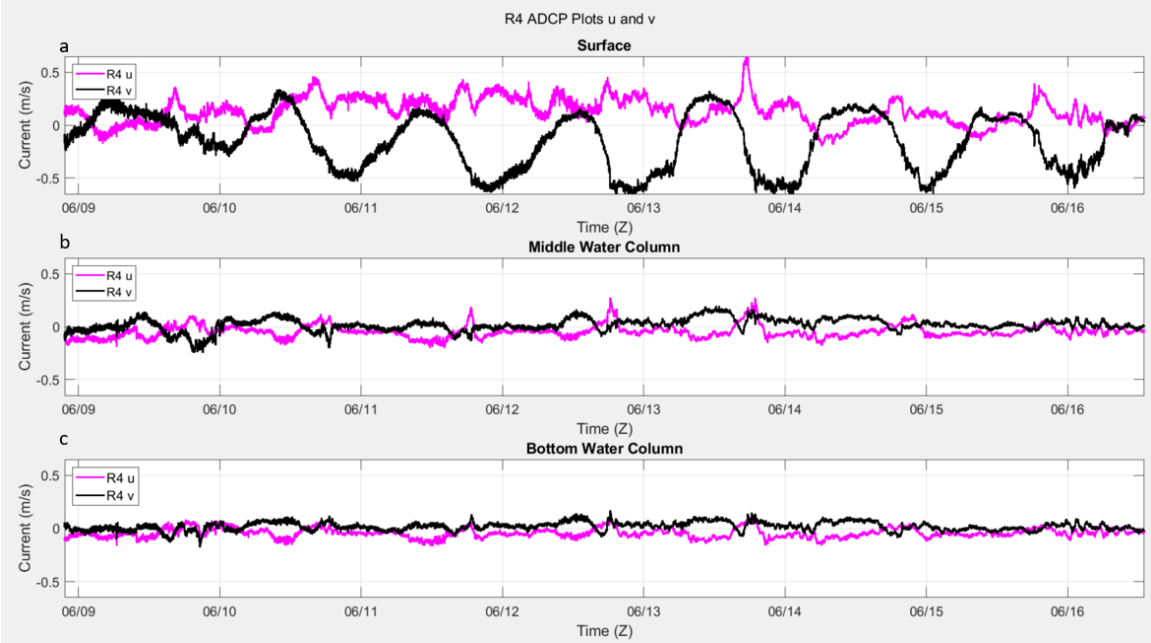

Figure 20. R4 ADCP plots for east/west (u) and north/south (v). Selected bin levels: a) Sfc = 8, b) Middle = 4, and c) Bottom = 1 based on 8 indices from the bottom to the surface.

C. ACOUSTIC DATA

Two different methods to determine signal to noise ratio in matched filtered data are typically used in the acoustic community. One is to use the peak pressure of the matched filter output (MFO) and subtract the nearby pressure that does not include the peak. A second is to integrate the energy over a small time window centered on the peak and subtract a similar sized window of integrated energy in the immediate vicinity of the peak. For this experiment, the first method was used. A moving average was computed, with a window size of 60 seconds to create power spectral density plots (PSD). This was done to determine the amount of energy at the receiver averaged over 60 seconds as a function of

frequency. Prior to matched filtering, the data were decimated to expedite processing and to narrow the resolvable frequency to focus on the L2MF signal. Data were decimated to make the sampling frequency (fs) 12,500 Hz, making the maximum resolvable frequency 6250 Hz.

Data were matched filtered in the 500–5000 Hz band. To find the peaks in each 2s window, the following three methods were used: "peakfinder," "max value," and "averaging" the strongest 75% of energy peaks over a 2 s window. After the first peak was identified manually and set as the initial location for the 2 s window, the window was then moved in 2 s intervals. The 2 s interval was selected due to this being the inter-pulse period of the transmitted signals, where a following peak was expected 2 s after each previous peak. Each of these methods was then used to develop plots to determine which method gave the best fit over the course of the transmitted period on June 9. Each of these three methods was evaluated with and without an envelope. After comparing results from the three methods, with and without an envelope, the maximum value without an envelope was determined as the best indicator throughout the period of transmission.

The peaks were visually inspected to ensure a valid signal was selected; any peaks not clearly associated with the LFM pulse annotated as Not a Number (NaN) in the result matrix. The LFM signal was not always able to be determined at the receiver due to background noise. At these times, AIS data from the United States Coast Guard (USCG) were used to validate whether a passing vessel had precluded an observable LFM pulse. This was done to ensure that only the transmitted signal was selected, and background noise, such as vessel traffic, would be removed from the dataset and replaced with a NaN. A spectral anomaly of each frequency was then computed.

IV. RESULTS

A. MODEL VERSUS DATA

Energy levels observed after the matched filtering were ~93 dB re 1µPa at R4 and ~84 dB re 1µPa at R3. While this was a nominal value overall, fluctuations on the scale of minutes are present. While there were multiple occasions where nulls were seen in the data, not all could be confirmed as a fluctuation due to the ebb plume front. One example of a null that correlated with the ebb plume front, which shows that the MFO amplitude at R3 decreased from ~87 to ~80 dB between 1811Z and 1818Z (Figure 21).

At R4, the signal fluctuated between received values of ~90 and ~95 dB re 1µPa at R4 during the transmission period. Values at R3 were lower than R4, due to its greater range from the source, and were measured at ~79-86 dB re 1µPa (Figure 21). Notably, the received energy levels between 1811Z and 1818Z at R3 decreased ~7 dB, while R4 did not experience a decrease.

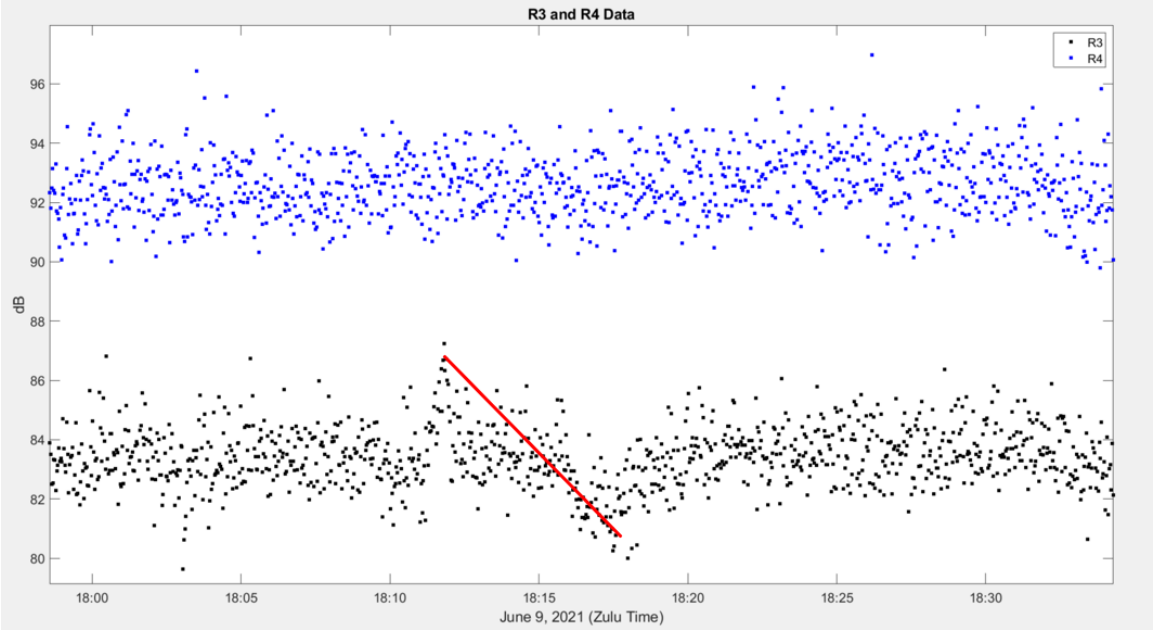

Figure 21. R3 and R4 data after MFO applied. Data is zoomed in on frontal passage, emphasized with the red line in R3 data.

Based on the frontal passage documented in the OSU radar data, this decrease appears to correspond to the passage of the bubble-laden ebb plume front IVO R3 (Figure 22).

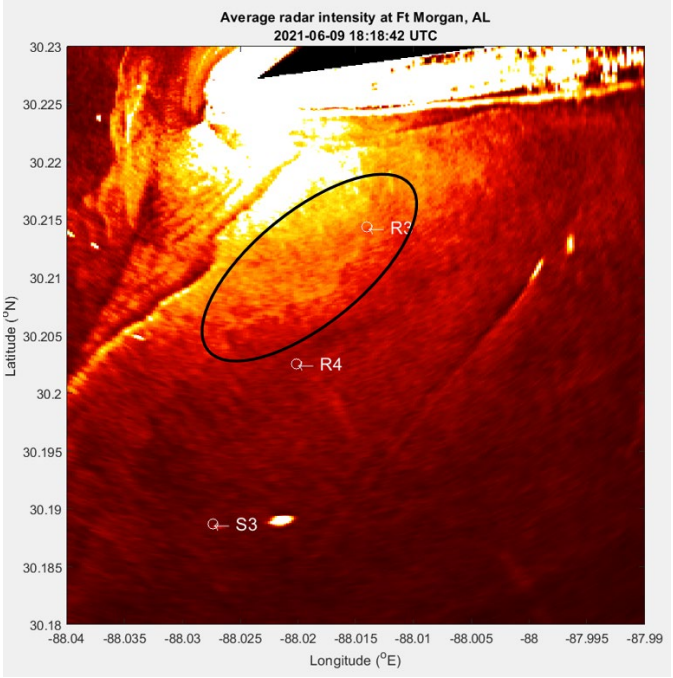

Figure 22. X-band radar image provided by OSU from June 9, 2021. Black ellipse emphasizes the location of the tidal front as passage over R3 occurs.

TL was modeled using Bellhop to compare model predictions to the level observed at the receiver locations. Bellhop model runs were set using nine rays, with launch angles of ±2 degrees from the x-axis. These parameters were set to have one ray every 0.5 degree, to keep the plot legible. Having parameters set to such low grazing angles prevented the appearance of BRSR rays, which experience elevated attenuation due to bottom loss and contribute the least to the observed acoustic energy at the receiver. TL values were taken as a point value for the receiver location, averaging 1%, 2%, 5%, and 10% of the cells for both depth and range surrounding the receiver location, as well as following the Harrison and Harrison (H&H) TL range-averaging model (1995) for each timestep. Averaging was conducted due to processing methods for the received signals being a MFO for a broadband

signal, while the input into Bellhop was a narrowband frequency of 2500 Hz. These values for averaging were selected to determine how comparable the modeled TL near the receiver location compared to collected data. After inputting the ROMS model predictions into Bellhop, the modeled TL results were obtained and placed into a matrix for each method based on the cells the receivers R3 and R4 were located at. For R3, 5% averages were comparable with the data until 1830Z, with the H&H method having minimal variation. This was likely due to H&H using a larger horizontal transect to average TL values around the receivers, causing the smallest variation over the source transmission period (Figure 23).

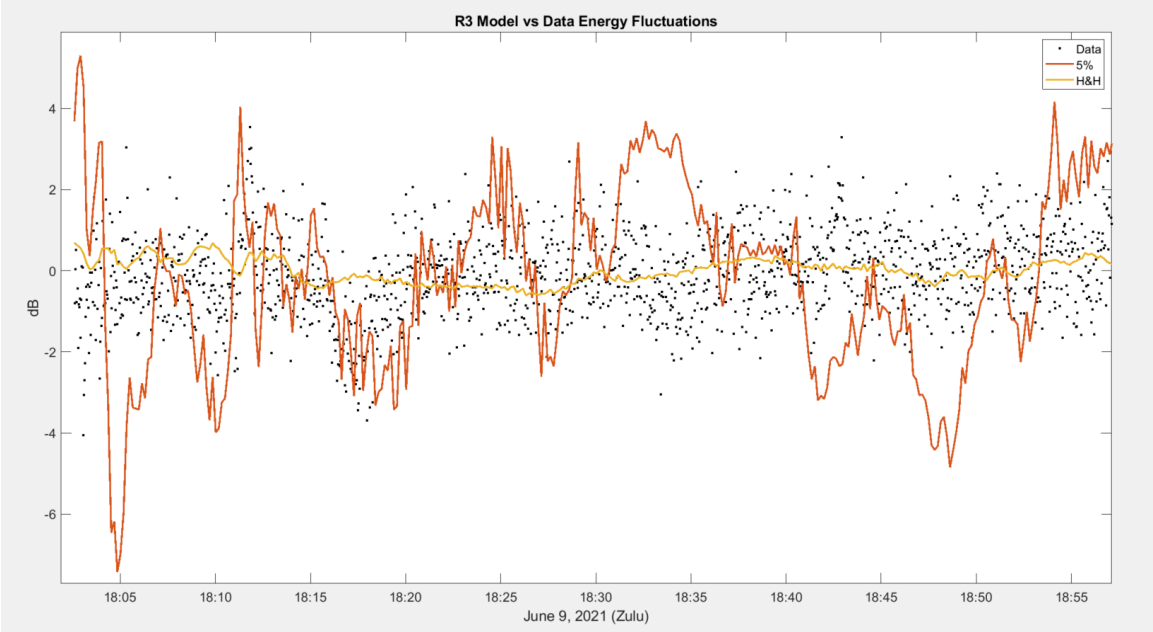

Figure 23. Bellhop model with inputs from the ROMs model reveals the existence of frontal passage ~1812Z. This passage of the front induced fluctuations in the transmission loss. Data were values measured from receiver at R3 1 meters above bottom (mab). All values were subtracted from mean values for equitable comparison.

Comparison of the MFO data with Bellhop TL results at R4 are shown in Figure 24. Due to R4 being closer to the source, and less affected by the water column,

there is less variability in modeled TL values, while the R4 data has similar nominal fluctuations as R3, without the larger decrease at ~1812Z.

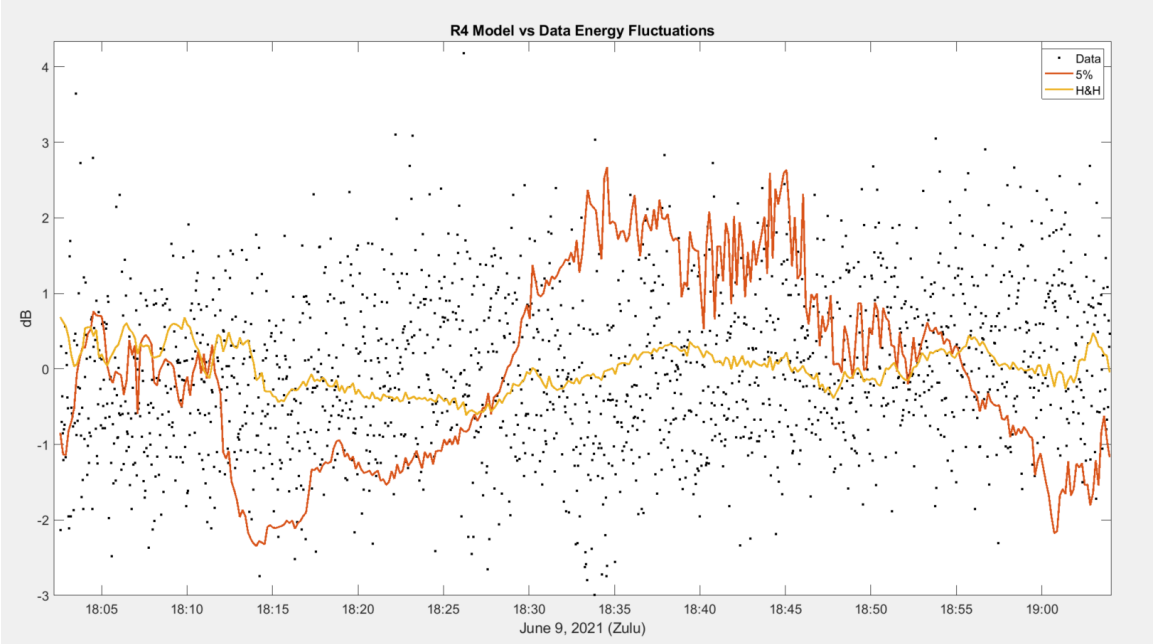

Figure 24. Bellhop model with inputs from the ROMs model for R4. Data is from the same time period as Figure 24. The tidal front has not crossed R4. All values were subtracted from mean values for equitable comparison.

Model output varied more than the data, in large part due to the observed datapoints are band averaged MFO of 1-second long LFM signals while the modeled output represents an instantaneous intensity at a single frequency. The H&H approximation shows very little variation due to the averaging window spanning a range equivalent to 87% of the acoustic transect.

Over the course of the tidal cycle, the ray traces demonstrate significant fluctuation. The water column structure changes as the ebb plume front passes over the acoustic transect, resulting in changes in the dominant propagation path. The top panel of Figure 25 shows that sound speeds are slower near the source and increase nearshore by R3. The modeled energy arrives via RBR, BRSR, and RSR paths. In the second panel, the ebbing tide causes the dominant path to shift to RBR, BRSR, RSR, and RR. The formation of the

RR path, indicated by the red line in the second panel, occurs only during approximately one hour of the tidal cycle. The RR path formation is caused due to warm fresh surface layer and cool salty bottom water cause a submerged sound channel (SSC) to form, centered on 3–3.5 m (Figure 25). This is due to the warm surface water creating a higher sound speed near the surface, while the salty deep layer increases sound speed near the bottom of the water column, creating a region of relatively slower sound speeds at 3–3.5 m. The highest sound speed occurs in a warm salt water region in the bottom right corner of panels 2 and 3. In the third panel, the dominant propagation path returns to RBR, BRSR, and RSR due to the sound speed gradient no longer being present.

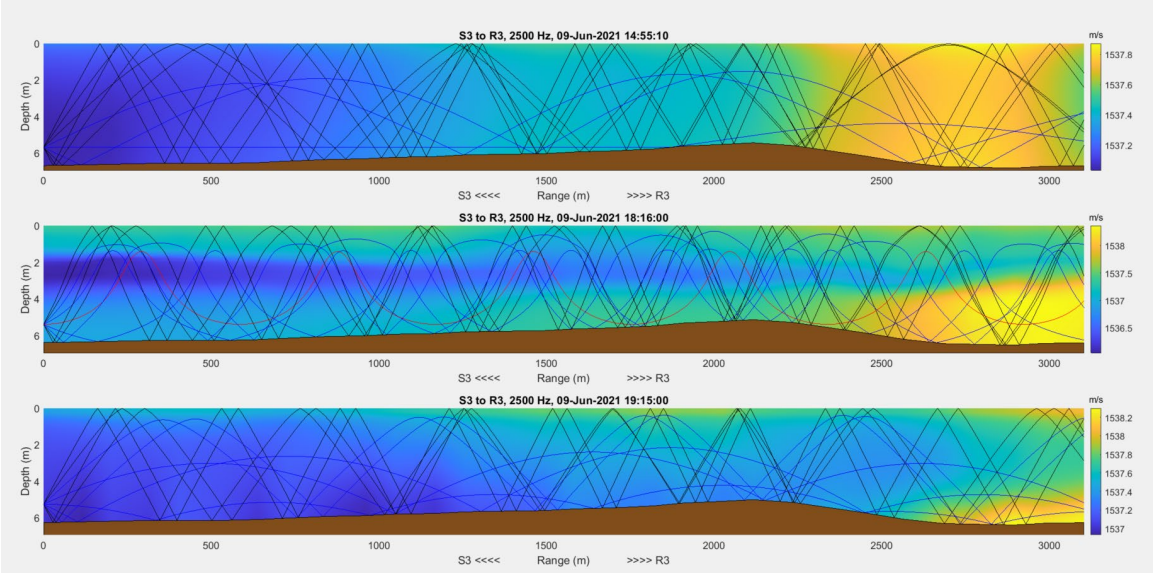

Figure 25. BELLHOP ray trace for source at 1 mab.

B. MODEL ACOUSTIC PROPAGATION IN SSC

During this first round of modeling, a duct was observed to form and then weakened over the tidal cycle (Figure 25). Figure 26 mirrors Figure 25 and illustrates the propagation characteristics of the waveguide in which the source depth is moved from 1 mab to the center of the SSC at 3 mab. Prior to the front passing, moving the source to 3 mab, the angles to interactions change, however the overall ray trace paths are similar. As the front passes, the number of rays trapped in the SSC changes. When the source is at 1 mab, only

one RR ray trace is trapped in the SSC. When the source is moved to 3 mab, six distinct rays become trapped in the SSC. After the front passes, the ray paths become similar to the source being at 1 mab again.

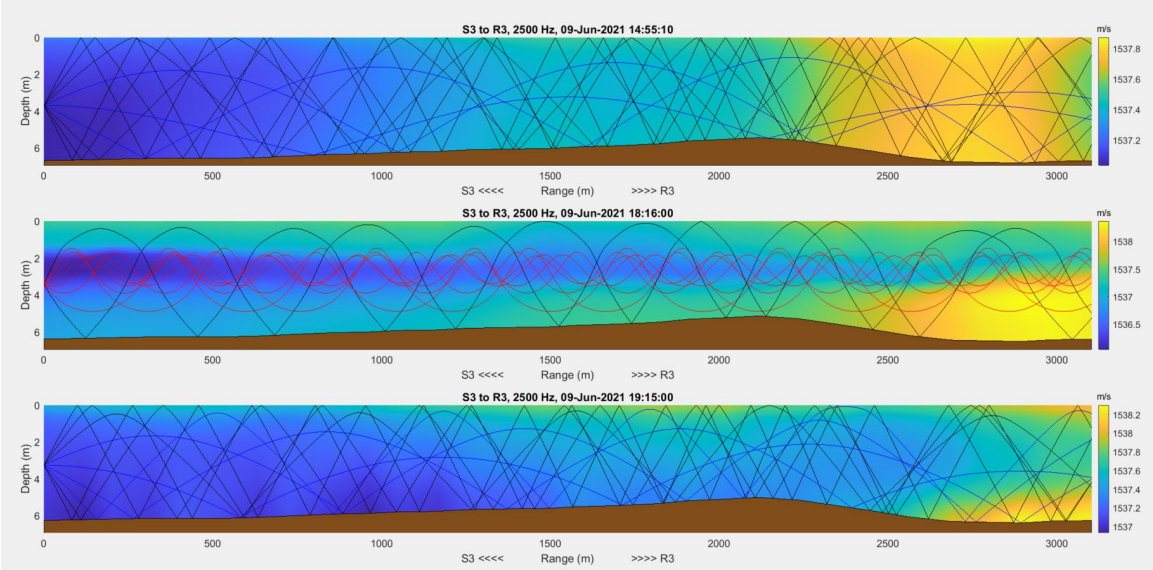

Figure 26. BELLHOP ray trace for source at 3 mab.

Model scenarios were rerun with the source level and receiver TL values being calculated to determine how TL would change in the duct over time. With the source moved from 1 mab to 3 mab, the energy can be seen focused along this sound channel axis once it formed (Figure 26). When compared to the model results with the source at 1 mab, the energy received at 1 mab depends more on the surface and bottom reflection; when the source is at 3 mab, the energy is primarily ducted in a narrow region of the water column with fewer boundary interactions.

C. MODELING BEFORE/DURING/AFTER FRONTAL PASSAGE

Three time periods were selected for the modeled salinity, temperature, sound speed, and TL. These times were chosen to examine the acoustic propagation (1) before frontal passage, (2) as the front passes the transect, and (3) after the front has passed the S3-R4-R3 acoustic transect. Prior to the frontal passage, the temperature is nearly

isothermal as a function of depth and range, with the warmer fresh water near the shore and cooler higher salinity IVO S3 (Figure 27; Figure 28). At the beginning of this tidal cycle, the water IVO R3 had temperatures ~2 ºC warmer than the waters around S3. As the tide ebbs, a warm and fresh layer of water forms in the upper 1–2 m of water and is visible in panel two. Once the ebb plume front has passed the acoustic transect, the water column becomes more nearly isothermal, with only ~0.5 ºC difference between the water near S3 and R3 (panel three).

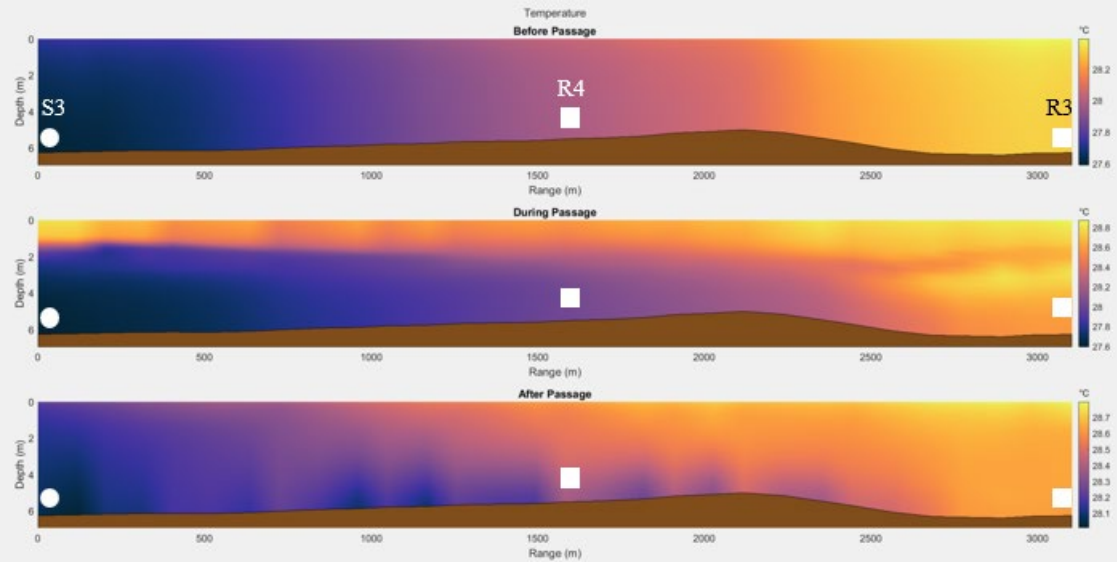

Figure 27. ROMS predicted temperature values before, during, and after tidal passage.

While warmer, fresher ebb plume water is present on the surface, cooler water with higher salinity remains at the bottom of the water column due to its higher density (Figure 28). The salinity experiences a similar effect as temperature, with the northern end of the transect remaining consistently ~1 PSU fresher before and after the tidal ebb, and a halocline persisting at 2–3 m depth as the tide ebbs.

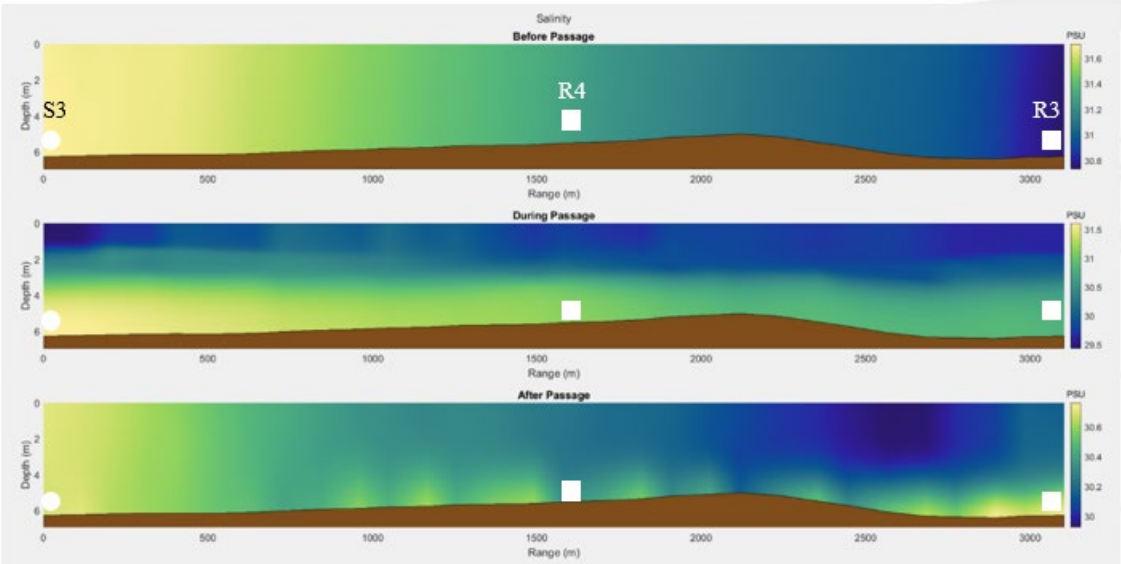

Figure 28. ROMS predicted salinity before, during, and after tidal passage.

Figure 29 shows the values for TL modeled by Bellhop based on the source depth of 1 mab (blue line) and 3 mab (red line). The modeled values for R3 are on the upper panels (a), with R4 values placed in the second row (b). Three distinct times were selected to emphasize changes in modeled TL based on the source depth changing. Prior to frontal passage where the water column is consistent, there are minimal fluctuations in modeled TL regardless of source depth. As the tide ebbs, the TL values begin to change, particularly near R3. These model fluctuations at R3 can change by as much as 17 dB when the source and receiver are at 1 mab. If the source and receiver are placed within the sound channel, the TL fluctuates by 10 dB at R3 (Figure 29). The signal at R4 does not experience as much fluctuation, likely due to being closer to the source and experiencing less environmental change over the shorter range. Less variation is shown in the modeled TL at R3 when the source is set at 3 mab than at 1 mab, and very little variation occurs at R4. Lower panels show modeled TL at R4 is consistently 10 dB less when the receiver and source are both in the SSC than when the source is at 1 mab. During the tidal transition, R3 model results show ~7 dB less loss during the tidal transition, likely driven by the SSC at 3 mab.

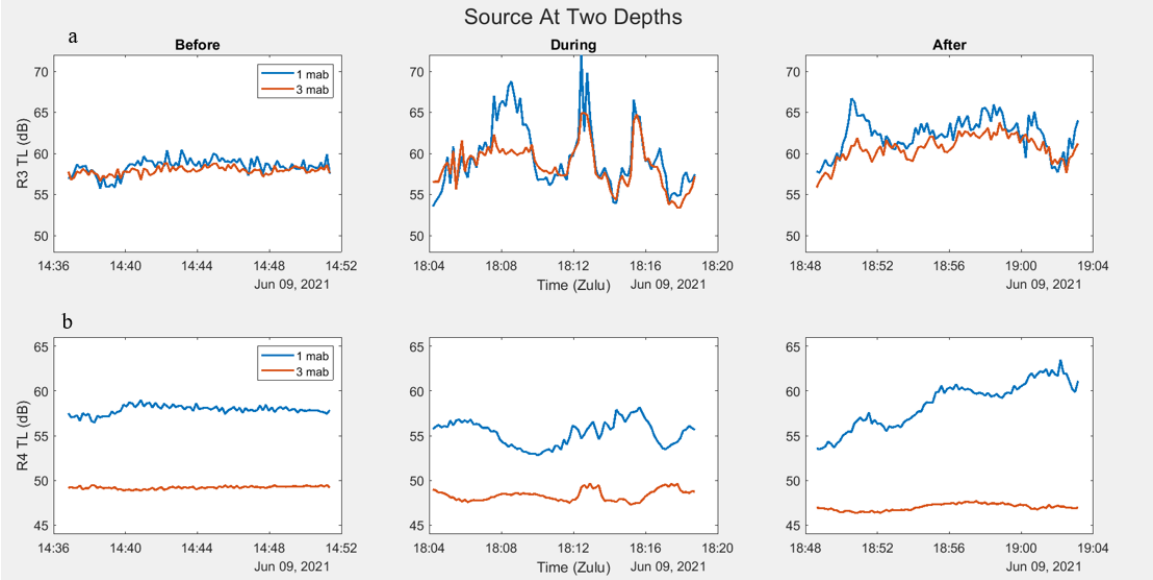

Figure 29. Model TL comparison at R3 and R4 at two source depths during the 20 min period centered on frontal passage. a) R3 model comparison based on source depth b) R4 model comparison. TL at R3 when source is at 3 mab TL ranges from ~55-65 dB, while at 1 mab TL ranges from ~54-72 dB.

THIS PAGE INTENTIONALLY LEFT BLANK

V. DISCUSSION

Salinity values measured by the Castaway CTD demonstrate consistent salinity values below 5 m and aligns with the data from the moored RBR-CTDs which experienced minimal fluctuations in salinity throughout the experiment (Figure 16). The comparison in sensors indicates that the surface fresh water layer never reached the receiver at 1 mab during any stage of the tidal cycle. The density difference in these two water masses can cause changes to the sound speed (Bascheck 2006). This surface fresh water thickness of 1–3 m has been seen in other estuaries, such as the Connecticut River (Reeder et al. 2018). Sound speed is calculated based on the temperature, salinity, and pressure. As any of these values increases, they will cause an increase in the sound speed (Lurton 2010). During the late spring season Mobile Bay has warm fresh water ebbing over cooler saltier water deeper in the water column. Since warmer and saltier water will cause an increase in sound speed, while the cooler and fresher water will cause the sound speed to decrease, the entrance of MOB experiences competing effects on the sound speed between these water masses. Due to these competing factors in sound speed, the sound speed gradient is very weak along the ebb plume front. With such a weak sound speed gradient, vertical and horizontal refraction at the front is expected to be non-observable (Reeder and Lin 2019). If this is the case, then the excess attenuation of 7 dB at R3 in the L2MF band during the ebb plume frontal passage may be attributable to attenuation by the bubble clouds in the ebb-plume front. While fresh water has a lower sound speed, the warmer temperature of this layer counters the slowing effect on sound speed. Since the surface fresh water layer is ~1 °C warmer than the water below, the temperature would cause refraction away from the surface. Because temperature impacts sound velocity more than salinity, the sound is refracted away from the surface during the summer months.

The cause of variance decreasing for the pressure sensor is likely due to winds early in the period being primarily SSE, shifting to WNW, seen in the color change in Figure 14. Throughout the experiment, winds were consistently between 4–10 m s^{-1}. While the wind speed is similar, the shift from SSE to WNW decreased the available fetch length to allow seas to develop and cause variance in the depth measurement to decrease. The changing

variance indicates that, although a similar wind speed occurs, the surface conditions can vary significantly (Novarini et al. 1998).

A large source of background acoustic energy in the water is the number and size of vessels in the region (Bassett et al. 2012). Typically, vessel noise is considered to dominate low frequencies in the 100s of Hz range (Leighton 1997; Lurton 2010). While this applies in the deep ocean, vessels in the nearshore environment contribute to broadband noise at higher frequencies, precluding L2MF signals at short range (Bassett et al. 2012; Reeder et al. 2020).

Transmission loss due to geometrical spreading is largely a function of range. Two mechanisms of TL are spherical spreading and cylindrical spreading; spherical spreading is parameterized as (Equation 1):

$$TL_{sphere} = 20\log_{10}(r) \tag{1}$$

Cylindrical spreading, in which sound is trapped by upper and lower boundaries, such as in a shallow water waveguide, is parameterized as (Equation 2) (Jensen et al. 1994):

$$TL_{cyl} = 10\log_{10}(r) \tag{2}$$

Spherical and cylindrical spreading are only two of the mechanisms which contribute to TL in an ocean waveguide; other loss mechanisms will contribute to actual, observed TL.

As model complexity increases, the TL estimate should become closer to the expected value. Two dimensional acoustic models consider vertical refraction, bottom loss, surface scattering, and account for spreading as a function of range (Ainslee 2005; Novarini et al. 1998). With Bellhop 2D, bottom sediment density, sediment attenuation, sediment sound speed, water column temperature, water column salinity, and source depth are considered (Porter 2019). Due to this, Bellhop accounts for all the expected 2D model parameters, and would be expected to output reasonable values for TL. While this includes more parameters, Bellhop 2D has been known to underpredict TL, likely due to ignoring diffraction, horizontal refraction, backscatter, or bubble clouds (Reeder and Lin 2019). Sediment appears consistent across the transect, however it may vary and could potentially

change loss values because Bellhop uses a single value for sediment density and sound speed. Although this may differ from real world data, the sediment in a transect will not change rapidly, and will consistently over or under predict TL caused by the bottom sediment. As such, it is reasonable to assume that increased TL at R3 during the period ~1815Z, with the tidal front passing R3, could be caused by a tidal bubble cloud.

ROMS models from S3-R3 were run at 10 s timesteps, with a horizontal resolution of ~90 m and a varying vertical resolution based on 15-layer profile. The values from the ROMS model were consistent with values measured with Castaway CTD data on June 9, 2021. Bubbles are known to cause significant increases in TL values at multiple frequencies (Ainslee 2005; Reeder et al. 2022) Model data shows instantaneous TL, which gives more variation over time than would be seen in the data. There are two methods to compare the modeled instantaneous TL with the real-world data, one is to use a band averaged method on a supercomputer, and the second is to use a single frequency (Harrison and Harrison 1995). Differences between modeled and collected data come from multiple details, including modeled data catching the front as desired, environmental data within the model being imperfect, and the depth of the sensor being below many of the bubbles. This resulted in a smaller portion of the front being sampled than in the model from S3-R3 and S3-R4.

A comparison of modeled spherical spreading, cylindrical spreading, 5% model, H&H model, and the observed TL are shown in Figure 30. Modeled TL for 5% and the H&H method both indicate losses between spherical spreading and cylindrical spreading. The modeled results are less than observed TL. The cause of the 30 dB disparity of the measured data and the modeled data comes from a variety of factors. The first is the assumption that the Lubell source was emitting at the programmed 180 dB re 1μPa at 1 m. If the source was not emitting at this high of an energy, the TL value would be less. A second factor for the difference in TL is due to the nature of the MFO result being an averaged value over the LFM pulse. This results in less energy being received than a narrowband signal measurement. A third factor that impacts the TL values is that the waveguide experiences more losses than modeled. This is expected due to surface interactions, estimated bottom roughness values, potential impacts of biological creatures

in the sediment, and bubbles near the surface causing refraction to the surface creating extra losses (Ainslee 2005; Hamilton 1980).

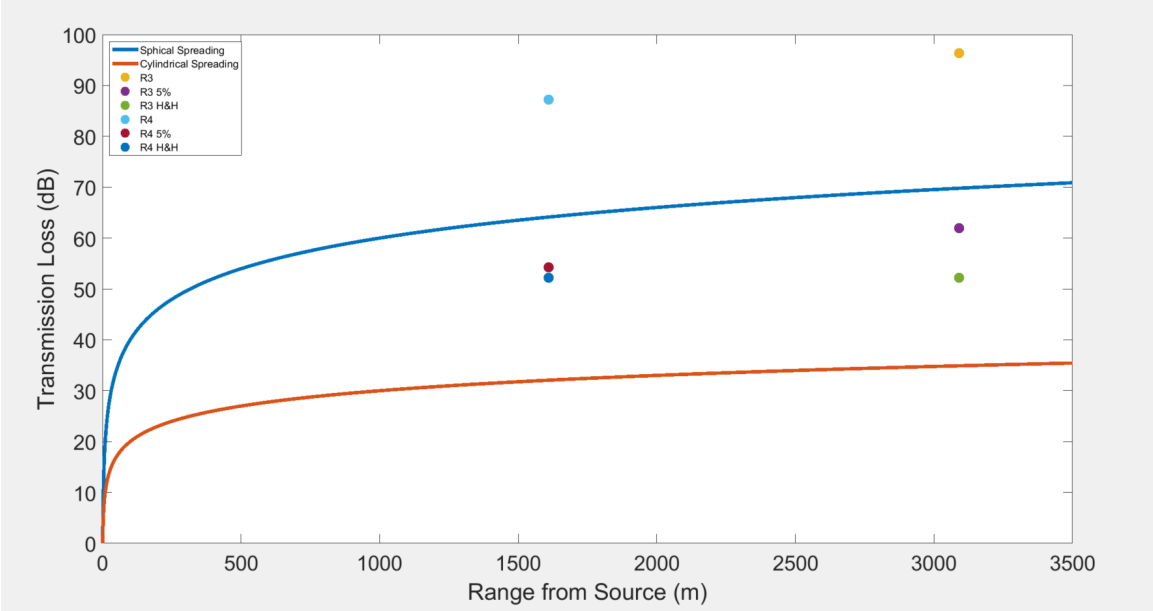

Figure 30. Transmission Loss based on calculated spreading, filtered data, and Bellhop modeled results.

Initially the ebb plume is ~2 m thick as it passes through the ROMS model. The ebb initially had a higher sound speed, due to its warmer temperature. This caused the sound propagation to initially be primarily RBR, BRSR, and RSR. As the front passes, and mixing occurs, sound speeds remain higher near the surface and the bottom. Fluctuations in the size and shape of the RBR path can be seen in the model on scales of a minute. This is most clearly reflected by Figure 21 where the signal can be seen to decrease at ~1817Z. The change in sound propagation path is caused by a tongue of slower water to develop ~1815Z. Slower sound speeds in the water column create an SSC, even though the water is less than 7 m deep. This sound channel creates a potentially exploitable region where ducting can occur.

There are a wide range of future projects that still require further research in the estuarine environment. While this thesis focused on a single narrowband frequency of 2500 Hz when comparing models between S3 and R3 outside the mouth of Mobile Bay,

exploring how S1 and R1 transmission compared inside MOB has yet to be conducted. A further step would be exploring different frequencies and comparing them to a measured broadband system to understand how multiple frequencies interact near the entrance of Mobile Bay. A gyre has been explained by Lee et al. (2019) but was not described with acoustic data during this experiment. Comparing the four different estuaries for L2MF propagation explored during the USRS program could provide similarities in propagation paths, regardless of the different physical environments experienced at each estuary. Shipping noise prevented reception of the L2MF signal during different periods of time and should be modeled to determine how shipping affects the structure of the water column over time to quantify these effects. The discovery of the duct indicates that work should be done with the source and receiver inside and outside the duct to determine how long the duct is available, as well as its exploitability.

THIS PAGE INTENTIONALLY LEFT BLANK

APPENDIX: FIELD LOG

CST	UTC	Log Entry
7-Jun-21		
0837	1337	Lines clear at Dauphin Island, Alabama
0940	1440	End coffin float test. Float test SAT
1009	1509	Begin deployment of coffin
1016	1516	Coffin fully deployed
1033	1533	Coffin recovered
1059	1559	Begin deployment of coffin
1105	1605	Coffin deployed
1125	1625	Mooring deployed
1128	1628	Mooring deployed
1135	1635	Mooing recovered
1140	1640	Coffin deployed
1200	1700	Coffin recovered
1234	1734	First line out at Dauphin Island, Alabama
8-Jun-21		
1108	1608	Start ADCP 7290 on R4
1116	1616	Start ADCP 7819 on R3
1340	1840	Lines clear at Dauphin Island, Alabama
1552	2052	R3 Deployed at 30°12.864'N 088°00.842'W
1636	2136	R4 deployed at 30°12.154'N 088°01.207'W
1742	2242	First line out at Dauphin Island, Alabama

9-Jun-21

0905	1405	Lines clear at Dauphin Island, Alabama
1051	1551	Coffin Deployed at S3 (30°11.324'N 088°01.641'W)
1059	1559	Lubell source turned on
1127	1627	Castaway CTD #1
1131	1631	Castaway CTD #2
1221	1721	Turn on over the side ADCP (serial number 2293) and Biosonics Echo Sounder
1226	1726	Tied to local oil rig, ship heading 020°
1251	1751	Sondecam in water
1338	1838	Castaway CTD #3
1334	1834	Lines clear of oil rig
1401	1901	Castaway CTD #4, ship drifting near S3
1441	1941	Stopped recording over the side ADCP
1442	1942	ADCP and Biosonics echo sounder aboard
1449	1949	Turned off Lubell source
1458	1958	Coffin aboard at S3
1600	2100	First line out at Dauphin Island, Alabama

10-Jun-21

0939	1439	Lines clear at Dauphin Island, Alabama
1004	1504	Lines out at DISL to get AAA batteries
1013	1513	Lines clear at DISL
1106	1606	Deploy coffin at S3
1112	1612	Turned on Lubell source

1212	1712	Found front
1215	1715	Over the side pole in place with ADCP and Biosonics Echo Sounder
1228	1728	Turned on ADCP. Ship heading ~310°
1404	1904	Bubbler (dBRd) deployed
1423	1923	Engines off, drifting ~290°
1442	1942	dBRd recovered, engines restarted
1500	2000	Crossed what appears to be front
1506	2006	dBRd deployed. Engines off. Heading ~250°
1513	2013	dBRd recovered, engines restarted
1519	2019	dBRd deployed. Engines off. Heading ~300°
1530	2030	dBRd deployed. Engines off. Heading ~284°
1537	2037	dBRd recovered, engines restarted
1543	2043	dBRd deployed. Engines off. Heading ~284°
1556	2056	dBRd recovered, engines restarted
1619	2119	Stopped ADCP and Biosonics echo sounder
1622	2122	Over the side pole onboard
1634	2134	Lubell turned “off,” but was already not transmitting
1644	2144	Coffin recovered
1659	2159	Transferred Acousonde to Craig McNeil on the R/V Gray Goose
1746	2246	First line out at Dauphin Island, Alabama

11-Jun-21

1002	1502	All lines clear at Dauphin Island, Alabama
1114	1614	Deploy R5 with Acousonde (A066) and RBR-CTD (205305) at 30°13.086’N 088°01.995’W

1138	1638	Deploy R2 with MAV (10307) at 30°13.587’N 088°01.870’W
		Deploy R1 with ADCP (2595), Acousonde (A050), MAV (10320), RBR-CTD (60318) at
1203	1703	30°14.806’N 088°01.932’W
1229	1729	Coffin deployed at S1 30°15.726’N 088°01.878’W
1230	1730	Lubell turned on
1244	1744	Over the side mount in water
1253	1753	Turned on ADCP and Biosonics Echo Sounder
1331	1831	Engines off
1233	1733	dBRd deployed
1336	1836	dBRd recovered
1342	1842	dBRd deployed. Engines off
1358	1858	Castaway CTD #5
1400	1900	dBRd recovered
1408	1908	dBRd deployed. Engines off.
1408-1418	1908-1918	CTDs 6–12
1418	1918	dBRd recovered
1514	2014	Over the side pole recovered
1543	2043	Lubell turned off
1549	2049	Coffin recovered
1645	2145	First line out at Dauphin Island, Alabama

12-Jun-21

0611	1111	Lines clear at Dauphin Island, Alabama
0630	1130	icListen on source #1422

0700	1200	Coffin deployed
0704	1204	Lubell turned on 30°15.746'N 088°01.823'W
0722	1222	Over the side mount in water
0729	1229	dBRd deployed. Engines off. Heading ~210°
0736	1236	dBRd recovered. Engines on.
0740	1240	dBRd deployed. Engines off. Heading ~215°
0741	1241	CTD #13
0748	1248	dBRd recovered. Engines on.
0759	1259	dBRd deployed. Engines off.
0809	1309	Lubell stopped producing sound
0819	1319	dBRd recovered. Engines on.
0825	1325	dBRd deployed. Heading ~230°
0825-0842	1325-1342	CTDs #29-43
0843	1343	dBRd recovered. Engines on.
0846	1346	dBRd deployed
0847-0854	1347-1354	CTDs #44-51
0857	1357	dBRd recovered
0905	1405	dBRd deployed. Heading ~227°
0905-0930	1405-1430	CTDs #52-79
0931	1431	dBRd recovered
0938	1438	dBRd deployed
0940-0954	1440-1454	CTDs #80-95
0951	1451	dBRd pulled in to get cable off CTD
0955	1455	dBRd recovered

1022	1522	dBRd deployed (1.5 meters down)
***		dBRd recovered
1038	1538	dBRd deployed (1.5 meters down)
1043-1050	1543-1550	CTDs #96-101
1052	1552	dBRd recovered
1057	1557	dBRd deployed (1.5 meters down)
1101-1105	1601-1605	CTDs #102-108
1107	1607	dBRd recovered
1118	1618	Over the side mount recovered
1134	1634	SVC off (not pinging)
1140	1640	Coffin recovered
1228	1728	First line out at Dauphin Island, Alabama

14-Jun-21

0746	1246	Lines clear at Dauphin Island, Alabama onboard R/V Caillou Boca
0833	1333	dBRd deployed (1.5m) Engines off. CTDs
0856	1356	dBRd recovered
0902	1402	dBRd deployed (1.5m) Engines off. CTDs
0956	1456	dBRd recovered
1008	1508	dBRd deployed (1.5m) Engines off. CTDs
1033	1533	dBRd recovered
1042	1542	dBRd deployed at surface. Engines off. CTDs
1138	1638	dBRd recovered
1157	1657	dBRd deployed. Engines off. CTDs

1224	1724	dBRd recovered
1306	1806	First line out at Dauphin Island, Alabama

15-Jun-21

0708	1208	Lines clear at Dauphin Island, Alabama
0742	1242	Over the side mount in water
0757	1257	dBRd deployed at surface. Engines stopped. CTDs
0841	1341	dBRd recovered
0900	1400	dBRd deployed. Engines stopped. CTDs
0922	1422	dBRd recovered
0935	1435	Fish jumping all around boat
0936	1436	dBRd deployed. Engines stopped. CTDs
1014	1514	dBRd recovered
1020	1520	dBRd deployed. Engines stopped. CTDs
1031	1531	dBRd recovered
1042	1542	dBRd deployed. Engines stopped. CTDs
1111	1611	dBRd recovered
1119	1619	dBRd deployed. Engines stopped. CTDs
1146	1646	dBRd recovered
1150	1650	dBRd deployed. Engines stopped. CTDs
1200	1700	dBRd recovered
1206	1706	Over the side mount recovered
1249	1749	First line out at Dauphin Island, Alabama

16-Jun-21

0656	1156	Cast off lines at Dauphin Island, Alabama
0732	1232	S2 recovered
0745	1245	R3 recovered
0808	1308	R4 recovered
0855	1355	R2 recovered
0919	1419	R1 recovered
0950	1450	First line out at Milk Shake Dock
1011	1511	Lines clear at Milk Shake Dock
1035	1535	First line out at Dauphin Island, Alabama

LIST OF REFERENCES

Ainslee, M.A., 2005: Effect of wind-generated bubbles on fixed range acoustic attenuation in shallow water at 1–4 kHz. *Acoust. Soc. Amer*, **118**, 3513–2523, https://doi.org/10.1121/1.2114527.

Baschek, B., D.M. Farmer, C. Garrett, 2006: Tidal Fronts and their role in air-sea gas exchange, *J. Mar. Res.*, **64**, 483–515.

Bassett, C., B. Polagye, M. Holt, J. Thomson, 2012: A vessel noise budget for Admiralty Inlet, Puget Sound, Washington (USA). *Acoustical Society of America*, **132**, 3706–3719, http://dx.doi.org/10.1121/1.4763548.

Bassett, C., J. Thomson, B. Polagye, 2013: Sediment-generated noise and bed stress in a tidal channel. *Journal of Geophysical Research*, **118**, https://doi.org/10.1002/jgrc.20169.

Bassett, C. and A. Lavery, 2021: Observations of high-frequency acoustic attenuation due to bubble entrainment at estuarine fronts. *Proceedings Acoustical Society of America*, Seattle, WA, **45**, https://doi.org/10.1121/2.0001539.

Blenkinsopp, C.E. and J.R. Chaplin, 2007: Void fraction measurements in breaking waves. *Proc. Roy. Soc. Lond.*, **463**, 3151–3170, https://royalsocietypublishing.org/doi/10.1098/rspa.2007.1901.

Chua, G., M. Chitre, G. Deane, 2018: Impact of persistent bubbles on underwater acoustic communication. *2018 Fourth Underwater Communications and Networking Conference (UComms)*.

Dahl, P.H., J.W. Choi, N.J. Williams, H.C. Graber, 2008: Field measurements and modeling of attenuation for near-surface bubbles for frequencies 1–20 kHz. *Journal of the Acoustical Society of America*, 124, https://doi.org/10.1121/1.2963096.

D'Amico, A. and R. Pittenger, 2009: A Brief History of Active Sonar. *Aquatic Mammals*, **35**, 426–434, https://doi.org/10.1578/am.35.4.2009.426.

Dzwonkowski, B., K. Park, J. Lee, B.M. Webb, A.Valle-Levinson, 2014: Spatial variability of flow over a river-influenced inner shelf in coastal Alabama during spring. *Continental Shelf Research*, **74**, 25–34, http://dx.doi.org/10.1016/j.csr.2013.12.005.

Farmer, D., 1984: The influence of bubbles on ambient noise in the ocean at high wind speeds. *Journal of Physical Oceanography*, **14**, 1762–1778.

Farmer, D., R. Pawlowicz, R. Jian, 2002: Tilting separation flows: A mechanism for intense vertical mixing in the coastal ocean. *Dynamics of Atmospheres and Oceans*, **36**, 43–58.

Flocks, J.G., N.T. DeWitt, and C.A. Stalk, 2017: Analysis of seafloor change around Dauphin Island, Alabama, 1987–2015. *Open-File Report*. https://doi.org/10.3133/ofr20171112.

Geyer, W.R. and P. MacCready, 2014: The estuarine circulation. *Annual Review of Fluid Mechanics*, https://doi.org/10.1146/annurev-fluid-010313-141302.

Gilday, M.M., Department of the Navy, 2021: CNO NAVPLAN 2021. July 14, 2022, https://media.defense.gov/2021/Jan/11/2002562551/-1/-1/1/CNO%20NAVPLAN%202021%20-%20FINAL.PDF.

Hamilton, E.L., 1980: Geoacoustic modeling of the sea floor. *Journal of the Acoustical Society of America*, **68**, 1313–1340, https://doi.org/10.1121/1.385100.

Harrison, C.H. and J.A. Harrison, 1995: A simple relationship between frequency and range averages for broadband sonar. *Journal of the acoustical Society of America*, **97**, 1314–1317.

Harrison, S.R., K.M. Koetje, A.M. Hode, C.B. DuVal, S. Dohner, E.E. Braithwaite III, J.C. Calantoni, 2021: *Bathymetry survey of the mouth of Mobile Bay, April 2021. Data description*. NRL-OP-7350-2021-5177.

Jensen, F.B., W.A. Kuperman, M.B. Porter, H. Schmidt, 1994: *Computational Ocean Acoustics*. American Institute of Physics, 612 pp.

Kim, C.K., and K. Park, 2012: A modeling study of water and salt exchange for a micro-tidal, stratified northern Gulf of Mexico estuary. *Journal of Marine Systems*, **96–97**, 103–115. https://doi.org/10.1016/j.jmarsys.2012.02.008.

Lamarre, E., W.K. Melville, 1991: Air entrainment and dissipation in breaking waves. *Nature*, **351**, 469–472.

Lee, J., B.M. Webb, B. Dzwonkowski, K. Park, and A. Valle-Levinson, 2013: Bathymetric influences on tidal currents at the entrance to a highly stratified, shallow estuary. *Continental Shelf Research*, **58**, 1–11. https://doi.org/10.1016/j.csr.2013.03.002.

Lee, J., B.M. Webb, B. Dzwonkowski, A. Valle-Levinson, and & J. Lee, 2019: Characteristics of exchange flow in a multiple inlet diurnal estuary: Mobile Bay, Alabama. *Journal of Marine Systems*, **191**, 38–50. https://doi.org/10.1016/j.jmarsys.2018.12.004.

Leighton, T.G., 1997: *The Acoustic Bubble*, Academic Press, 613 pp.

Lurton, X., 2010, *An Introduction to Underwater Acoustics Principles and Applications*. 2nd ed., Springer, 680 pp.

Lyzenga, D.R., 1991: Interaction of short surface and electromagnetic waves with ocean fronts. *J. Geophys. Res*, **96(C6)**, 10765-10772. https:///doi.org/10.1029/91JC00900.

McDaniel, S.T. and A.D. Gorman, 1982: Acoustic and radar sea surface backscatter. *Journal of Geophysical Research*, **87**, 4127–4136.

Medwin, H., 2005: *Sounds in the Sea: From Ocean Acoustics to Acoustical Oceanography*, Cambridge University Press, 643.

Novarini, J.C. and D.R. Bruno, 1982: Effects of the sub-surface bubble layer on sound propagation. *Journal of the Acoustical Society of America*, **72**, 510–514, https://doi.org/10.1121/1.388107.

Novarini, J.C., R.S. Keiffer, and G.V. Norton, 1998: A model for variations in the range and depth dependence of the sound speed and attenuation induced by bubble clouds under wind-driven sea surfaces. *Journal of Oceanic Engineering*, **23**, 423–438.

Orescanin, M.M., S. Elgar, B. Raubenheimer, 2016: Changes in bay circulation in an evolving multiple inlet system. *Continental Shelf Research*, **124**, 13–22, http://dx.doi.org/10.1016/j.csr.2016.05.005.

Porter, M.B., 2019: *The BELLHOP Manual and User's Guide*. Heat, Light, and Sound Research, Inc.

Ralston, D.K., G.W. Cowles, W.R. Geyer, R.C. Holleman, 2017: Turbulent and numerical mixing in a salt wedge estuary: dependence on grid resolution, bottom roughness, and turbulence closure. *Journal of Geophysical Research: Oceans*, **122**, 692–712, https://doi.org10.10002/2016JC011738.

Ralston, D.K., 2022: Impacts of storm surge barriers on drag, mixing, and exchange flow in a partially mixed estuary. *Journal of Geophysical Research: Oceans*, **127**, https://doi.org/10.1029/2021JC018246.

Reeder, B., 2016: Field observation of low-to-mid-frequency acoustic propagation characteristics of an estuarine salt wedge. *Journal of the Acoustical Society of America*, **139**, 21–29, https://doi.org/10.1121/1.4939108.

Reeder, B., D. Honegger, J. Joseph, C. McNeil, T. Rago, D. Ralston, 2018: Acoustic propagation at low-to-mid-frequencies in the Connecticut River, *Proceedings Acoustical Society of America*, Minneapolis, MN, **33**, https://doi.org/10.1121/2.0000811.

Reeder, B. and Y.T. Lin, 2019: 3D acoustic propagation through an estuarine salt wedge at low-to-mid-frequencies: Modeling and measurement, *J. Acoustic Society of America*, **146**, 1888–1902, https://doi.org/10.1121/1.5125258.

Reeder, B., Y.J. Yang, S. Ramp, S. Jan, and M.H. Chang, 2019: Near-surface underwater sound generated by internal solitary waves in the South China Sea. *J. Acoustic Society of America*, **146(4),** 3027.

Reeder, B., J.E. Joseph, T.A. Rago, 2020: Underwater sound generated by motor vehicle traffic in an underwater tunnel, *J. Acoustic Society of America*, **148**, EL215-EL220, https://doi.org/10.1121/10.0001805.

Reeder, B., J.E. Joseph, T.A. Rago, J.M. Bullard, D. Honegger, M.C. Haller, 2022: Acoustic spectrometry of bubbles in an estuarine front: Sound Speed dispersion, void fraction, and bubble density, *J. Acoustic Society of America*, **151**, 2429–2443, https://doi.org/10.1121/10.0009923.

Rogers, J.A., 2020: *Bubble cloud acoustic spectrography in the James River estuary*, Oceanography, Naval Postgraduate School, 75.

Schroeder, W.W., S.P. Dinnel, and W.J. Wiseman Jr, 1990: Salinity stratification in a river-dominated estuary. *Estuaries*, **13**, 2, 145–154, https://www.jstor.org/stable/1351583.

Thurman, E., J. Riordan, and D. Toal, 2013: Real-time adaptive control of multiple collocated acoustic sensors for an unmanned underwater vehicle. *Journal of Oceanic Engineering*, **38**, 419–432.

Urick, R.J., 1996, Peninsula Pub, *Principles of Underwater Sound.* 3rd ed. Peninsula Pub, 423 pp.

USCG, 2022: Vessel traffic data. Accessed 24 August 2022, https://marinecadastre.gov/ais/.

Warner, J.C., W.R. Geyer, J.A. Lerczak, 2005: Numerical modeling of an estuary: A comprehensive skill assessment. *Journal of Geophysical Research*, **110**, https://doi.org/10.1029/2004JC002691.

THIS PAGE INTENTIONALLY LEFT BLANK

INITIAL DISTRIBUTION LIST

1. Defense Technical Information Center
   Ft. Belvoir, Virginia

2. Dudley Knox Library
   Naval Postgraduate School
   Monterey, California